The Pennsylvania State University

The Graduate School

Department of Materials Science and Engineering

Piezoelectric and Dielectric Reliability in Lead Zirconate Titanate Thin Films

A Thesis in

Materials

by

Ronald G. Polcawich

©1999 Ronald G. Polcawich

Submitted in Partial Fulfillment
of the Requirements
for the Degree of

Master of Science

August 1999

I grant The Pennsylvania State University the nonexclusive right to use this work for the University's own purpose and to make single copies of the work available to the public on a not-for-profit basis if copies are not otherwise available.

Ronald G. Polcawich

We approve the thesis of Ronald G. Polcawich.

Date of Signature

Susan Trolier-McKinstry — 7-14-99
Associate Professor of Ceramic Science and Engineering
Thesis Advisor
Chair of Committee

Clive A. Randall — 7/13/99
Associate Professor of Materials Science and Engineering

William L. Warren — 7/10/99
Program Manager, Defense Advanced Research Project Agency
Special Signatory

Robert N. Pangborn — 7/14/99
Professor of Engineering Mechanics
Head of Intercollege Graduate Program in Materials

Abstract

Lead zirconate titanate ($PbZr_xTi_{1-x}O_3$) thin films offer higher piezoelectric constants and electromechanical coupling coefficients than ZnO, and as a result are extremely attractive for MEMS applications. To date, though, there is little data on the reliability of these materials as actuators under high electric field drive conditions. Thus, this thesis was directed towards developing a database for the long-term reliability of the transverse piezoelectric coefficient, d_{31}, under both unipolar and bipolar drives. Under unipolar drive, the films show excellent reliability with devices exhibiting increasing piezoelectric constants over time due to progressive poling of the capacitors. Under these conditions, 99% of the ~1.0 μm thick capacitors examined survived to 10^9 cycles at electric fields of 120 – 200 kV/cm. Aging rates between 6 and 12% per decade were typical for normally poled PZT thin films. A reduction in the net polarization, possibly depoling due to an internal electric field, was responsible for the rapid aging rates. Even faster degradation occurred during low field bipolar operation with losses as great as 50 % witnessed after 10^9 cycles. Similar to the aging results, a field induced depoling mechanism was responsible for the large degradation in the piezoelectric constant during cycling.

Thermal and ultraviolet imprint techniques were used to improve aging and bipolar drive reliability. For films poled at 150°C, defect dipole alignment reduced aging to 2 - 4 %/decade, which is similar to the aging of the dielectric constant. Low field bipolar drive on thermally imprinted devices resulted in slightly increasing piezoelectric coefficients. Ultraviolet illumination also improved both aging and bipolar degradation.

UV illumination resulted in non-linear aging due to the presence of an internal space charge field that develops from photo-induced charge carriers. As the space charge field decays over time, d_{31} increases until $10^5 - 10^6$ seconds after poling at which time d_{31} remains constant or slightly declines. Thus, the changes in d_{31} were confined to 3 – 5 % at 10^6 seconds after poling. Similar behavior occurred during bipolar operation with minimal changes in the piezoelectric coefficient after 10^9 cycles.

Additionally, a series of highly accelerated lifetime tests (HALT) was performed to determine the dc reliability of PZT thin films. Statistical analysis was performed on sets of 30 samples that were tested at temperatures ranging from 120°C to 180°C and voltages ranging from 25 V to 40 V. A graphical analysis of the results, assuming a lognormal distribution, revealed that breakdown was due to two distinct failure modes, early freak failures due to extrinsic defects and later failures that exhibit a rapid increase in leakage current upon breakdown. Additionally, the analysis provided numerical values for the median time to failure, t_{50}, and standard deviation of the distribution of failure times, σ_{ln}. The value of σ_{ln} for various voltage and temperatures stresses remained similar with slight variations possibly due to the limited sample size. The relative independence of this parameter allowed for a direct determination of the activation energy for failure, ~0.78 eV, and voltage acceleration factor, ~7.8. Lastly, samples that failed during the HALT experiments were analyzed by scanning electron microscopy. Analysis revealed that microcracking, film/electrode delamination, and arcing all contribute to failure during operation.

Table of Contents

List of Figures VII
List of Tables XI
Acknowledgements XII
Chapter 1: Introduction 1
Chapter 2: Literature Survey 3
2.1 Introduction 3
2.2 Ferroelectric Materials 3
2.2.1 Phenomenology 7
2.3 Lead Zirconate Titanate (PZT) 11
2.3.1 Hard and Soft PZT Ceramics 12
2.3.2 PZT Thin Films 13
2.4 Piezoelectricity 14
2.4.1 Direct and Converse Piezoelectric Effect 14
2.4.2 Intrinsic and Extrinsic Contribution to the Piezoelectric Effect 16
2.5 Microelectromechanical System (MEMS) 18
2.5.1 Thin Film MEMS Devices 19
2.5.2 MEMS Design 20
2.6 Degradation Mechanisms 21
2.6.1 Bulk Ceramics 21
2.6.2 Thin Films 29
Chapter 3: Experimental Procedure 32
3.1 Film Production 32
3.2 Electrical Contacts 33
3.3 High and Low Field Ferroelectric and Dielectric Characterization 34
3.4 Measurement of the Transverse Piezoelectric Coefficient 35
3.5 Reliability of PZT Films Under ac Electric Field Drive 36
3.6 Imprint of PZT Films 36
3.7 HALT Measurements 37
3.8 Dielectric Breakdown 37
3.9 Degradation Mechanism Characterization 38
Chapter 4: Results and Discussion 39

4.1 Introduction 39
4.2 Ferroelectric, Dielectric, and Piezoelectric Properties 39
4.3 Aging 40
4.4 Affect of a Unipolar ac Electric Field 42
4.5 Bipolar ac Electric Field Drive 45
4.6 Imprint to Improve Reliability 47
4.6.1 Affect of Imprint on Aging 49
4.6.2 Affect of Imprint on Bipolar Degradation 58
4.7 HALT Analysis 62
4.8 Microscopy Analysis of Device Failure 68
4.8.1 Scanning Electron Microscopy 68
4.8.2 Auger Electron Spectroscopy 72
Chapter 5: Conclusions & Future Work 73
5.1 Conclusions 73
5.2 Recommendations for Future Work 76
5.2.1 Develop Database for HALT Analysis on PZT Thin Films 76
5.2.2 Ellipsometry as a Means of Measuring Oxygen Concentrations 76
5.2.3 Bombardment Induced Imprint 77
5.2.4 Verification of a Photovoltaic Induced Internal Electric Field 78
5.2.4 Modeling Aging Behavior through a Modified Activation Barrier 79
5.2.5 Magnitude of Internal Electric Field as a Function of Unipolar Cycles 80
Appendix 81
References 84

List of Figures

Figure 2.1: Representation of the cubic (Pm3m) prototype structure of perovskite ABO_3 structure. 4

Figure 2.2: Lattice distortions that occur upon cooling below T_c in perovskites: a) In the tetragonal phase, P_s develops along [001] of the original cubic structure, b) in the orthorhombic phase, P_s occurs along [011], and c) in the rhombohedral phase, P_s develops along [111]. The dotted cubes are for the cubic prototype; the solid lines show the distorted unit cells of the ferroelectric phases. 5

Figure 2.3: Schematic of the polarization electric field hysteresis loop illustrating the saturation polarization (P_{sat}), remanent polarization (P_r), and coercive field (E_c). 5

Figure 2.4: Possible polarization directions relative to the cubic prototype for a) tetragonal perovskite with 6 equivalent <001> directions, b) orthorhombic distortion with 12 equivalent <110> directions, or c) rhombohedral with 8 equivalent <111> directions. 6

Figure 2.5: Phase diagram for the lead zirconate - lead titanate solid solution. 11

Figure 2.6: Variation in relative permittivity and piezoelectric coupling coefficient (k) with variation in the Zr/Ti ratio for PZT ceramics. 12

Figure 2.7: The direct and converse piezoelectric effects. (a) The direct effect is the generation of a surface charge, Q, upon the application of an applied stress, X. In this depiction, the d_{333} coefficient is presented with the stress applied on the 1-2 plane in the 3 direction and the generated charge accumulates along the 3 direction. (b) The converse effect is the dimensional change of the material, or strain, x, upon the application of an electric field. This schematic illustrates both a contraction along the 3 direction using d_{333} and expansions in the 1 and 2 directions by d_{311} and d_{322}. 15

Figure 2.8: Temperature dependence of the dielectric constant and transverse piezoelectric coefficient for 4 different bulk compositions of PZT. Types 1 and 3 are hard PZTs doped with NiO and Fe_2O_3, respectively. Types 2 and 4 are soft PZT doped with Nb_2O_5 and Sb_2O_3, respectively. 17

Figure 2.9: Scanning electron micrographs of a) a micro slide motor constructed of polysilicon and b) a micro motor constructed of permalloy. 18

Figure 2.10: Scanning electron micrographs of a) a micropump and b) a microvalve using PZT thin films as the actuator. 19

Figure 2.11: Schematic of a) a cantilever beam and b) a diaphragm design for piezoelectric MEMS devices. 20

Figure 2.12: Degradation of a) switchable polarization, b) permittivity, and c) transverse piezoelectric coefficient as a function of bipolar electrical cycles in PZT bulk ceramics. Fatigue degradation occurs in each property and the same electric field dependence is witnessed for each property. 23

Figure 2.13: Piezoelectric reliability in PZT bulk ceramics during unipolar drive.......... 24

Figure 2.14: Delamination at the electrode ceramic interface in a multilayer actuator. ... 25

Figure 2.15: Microcrack initiation at the termination of an internal electrode of a multilayer actuator.......... 26

Figure 2.16: Schematic of electric field impingement in the vicinity of a pore.......... 26

Figure 2.18: Illustration of the I-t curves typical for ABD and TRA type failures.......... 28

Figure 2.19: Aging of the longitudinal piezoelectric coefficient and the dielectric constant for a) a PZT thin film and b) a PZT ceramic.......... 30

Figure 3.1: Schematic of the electrical connections used in making contact with the capacitors and performing dielectric and piezoelectric measurements. During cycling an ac voltage is applied to each sample using a buffer microchip to ensure a stable signal. By changing the connections to the HI and LO lines, ferroelectric, dielectric, and piezoelectric properties of individual capacitors could be measured. . 34

Figure 3.2: Schematic of the wafer flexure method. A PZT-coated Si wafer is clamped between Al rings (not to scale).......... 36

Figure 4.1: Polarization electric field hysteresis loop for a 1.0 μm thick PZT (52/48) thin film.......... 40

Figure 4.2: (a) Aging of the absolute value of d_{31} and (b) aging of the dielectric permittivity, ε_{33}, and the transverse piezoelectric coefficient, d_{31}.......... 41

Figure 4.3: Characteristic changes in the d_{31} and ε_{33} coefficient during unipolar cycling with a maximum electric field of 3 and $5E_c$ (~120 - ~200 kV/cm). Error bars illustrate the range of values obtained in several experiments.......... 42

Figure 4.4: Shift in the polarization electric field hysteresis loop after unipolar drive at 200 kV/cm. The magnitude of the shift is 4.9 kV/cm.......... 43

Figure 4.5: Representative results for PZT thin films with low breakdown fields (~250 kV/cm) cycled with a unipolar field of 200 kV/cm. Ranges given show sample-to-sample variations.......... 45

Figure 4.6: Amplitude dependence of bipolar degradation with each curve representing the typical behavior observed at a specified cycling field. The strong amplitude dependence indicates field induced depoling is the mechanism responsible for the decrease in d_{31} with cycling. The ranges given are indicative of sample-to-sample variability.......... 46

Figure 4.7: Schematic of the detrapping of electronic charges through the use of ultraviolet illumination during poling. Removal of the space charge at the domain boundaries allows locked domains to align with the applied electric field.......... 48

Figure 4.8: Schematic illustrating the use of thermal energy during poling to produce imprint in PZT thin films. The thermal energy allows the defect dipole complexes ($V_{Pb}'' - V_O^{\bullet\bullet}$, $Fe_{Ti}' - V_O^{\bullet\bullet}$, etc.) to align with an applied electric field. Upon removal of the field the defect dipoles pin the domains in the new aligned configuration.......... 49

Figure 4.9: Imprint effects on aging. Thermal imprint reduces the aging rate from 7 – 10 %/decade to 2 – 3 %/decade. UV imprint results in non-linear aging because of an internal space charge field. ... 50

Figure 4.10: Affect of thermal imprint on the temperature dependence of ε_{33}. Differences in the room temperature dielectric properties for thermally imprinted and normally poled films are eliminated at 4 Kelvin. ... 51

Figure 4.11: Aging of ε_{33} and d_{31} for a thermally imprinted sample illustrating nearly identical aging rates. ... 52

Figure 4.12 : Comparison of the voltage shifts in the PE loop of UV and thermally imprinted thin films. ... 53

Figure 4.13: Changes in the piezoelectric response in response to UV illumination. Prior to exposure, the device ages at 7 %/decade. Upon illumination, there is a sharp decline in d_{31} in response to a depoling mechanism. Subsequent decreases are the result of the build up of a space charge field. After illumination, d_{31} again drops but then begins to rise as the space charge field diminishes. Error bars are representative of the range of values observed among several similar experiments. . 55

Figure 4.14: Schematics illustrating the mechanisms responsible for the aging behavior of UV exposed samples: (a) initial normally poled sample with the applied field (E_{app}) directed toward the bottom electrode, (b) photo-excitation of charge carriers by UV illumination, (c) metastable domains back-switch, aligning with depolarization field (E_{dep}), (d) migration of photo-induced charge carriers, resulting in a photoelectric field (E_{ph}), (e) development of an internal space charge field due to a charge carrier concentration gradient ($E_{gradient}$), (f) decay of the internal field due to migration and recombination of excess charge carriers. ... 56

Figure 4.15: Affect of imprint on bipolar degradation illustrating the observed trends for each of the poling procedures. ... 59

Figure 4.16: Characteristic changes in d_{31} and ε_{33} during bipolar operation (~20 kV/cm) for thermally imprinted 1.0 μm thick PZT films. ... 60

Figure 4.17: PE loops prior to and after bipolar operation. ... 60

Figure 4.18: PE loop illustrating that a 20 kV/cm (shaded region) bipolar field provides a smaller degree of polarization switching in imprinted devices compared to normal devices. ... 61

Figure 4.19: Plot of leakage current versus the time illustrating that failure occurs as an abrupt increase in the leakage current ... 63

Figure 4.20: Cumulative percent failure plot for HALT test conducted with a field of 250 kV/cm and at a temperatures of 180°C. ... 64

Figure 4.21: Plot of MTF versus 1/T determining the activation energy for failure. From the slope of the line, an E_a of 0.78 eV is calculated. ... 66

Figure 4.22: Plot of MTF versus voltage yielding a voltage acceleration factor of 7.8.... 67

Figure 4.23: Scanning electron micrograph of cracking and delamination ... 68

Figure 4.24: SEM micrograph of arcing revealing that the discharge region is riddled with tiny spheres of material. 69

Figure 4.25: Edge of arcing region showing the PZT film wrapped over itself, possibly due to peeling from the magnitude of stresses or a flash melting event. 70

Figure 4.26: Results from energy dispersive spectroscopy on various regions in and around the arcing region. 71

Figure 4.27: Results from Auger electron depth profiling on both a virgin sample and a sample driven at 400 kV/cm for 48 hours. Although all components of the PZT films were analyzed, the above plot only presents the results for platinum, lead, and oxygen. 73

Figure A.1: Plot illustrating an S-shaped cdf curve and the graphical technique used to determine t_{50} and σ_{ln}. 83

List of Tables

Table 2.1: Thermodynamic potentials for a polarizable deformable solid with the boundary conditions for each potential. The independent variables are temperature (T), stress (X_{ij}), and electric field (E_m) while the dependent variables are polarization (P_m), strain (x_{ij}), and entropy (S).[12] 8

Table 2.2: Thermodynamically derived definitions of the four piezoelectric coefficients: d_{mij}, g_{mij}, e_{mij}, h_{mij}.[12] 10

Table 4.1: Results from HALT tests. Times are in hours. 65

Acknowledgements

I would like to thank Dr. Susan Trolier-McKinstry for the opportunity of completing my graduate studies at the Pennsylvania State University and her tutelage over the past two years. I would also like to thank my committee members, Dr. Clive Randall and Dr. William Warren, for their sage advice. A great deal of thanks must also be extended to Dr. Stewart Kurtz for his tutelage on statistical reliability and Dr. Cheng-Ning Feng for his assistance during the HALT measurements.

Over the past two years, there have been many individuals that have provided me with support and knowledge. Primarily, I would like to acknowledge DARPA (contract DABT63-95-C-0053) and NSF (contract DMR-9502431) for the funding they provided. I would also like to thank the past and current members of the STM research group. Mark Angelone and Vince Bojan should be commended for their assistance in obtaining EDS and AES results. I would like to thank Paul Moses for his assistance on the electrical circuitry involved with the measurement equipment. Additionally, the entire MRL staff should be commended for their hard work and devotion to helping the faculty and students conduct the best research possible.

Most importantly, I could not have completed my graduate work without my friends and family. Everyone from new friends to old have supported my endeavors and encouraged me to perform at the highest level. Specifically, I need to thank my roommate and long time friend, Marc Palmisiano, for not only companionship but also great intellectual discussions on the finer points of materials engineering. Not to be forgotten, I would like to thank my family and my loving girlfriend, Margaret Powers, for their support and love.

Chapter 1: Introduction

Interest in device miniaturization has led to the desire for thin films with large piezoelectric coefficients for sensors, actuators, and microelectromechanical systems (MEMS). One of the leading candidate materials for these devices is lead zirconate titanate (PZT) because its piezoelectric coefficients are an order of magnitude larger than those of widely used materials like aluminum nitride (AlN) and zinc oxide (ZnO).[1, 2] As PZT-based microdevices are developed, reliability issues became of great concern. However, only a limited number of studies have focused on electromechanical reliability and the mechanism(s) responsible for degradation in films.

A majority of the studies to date focused on determining the reliability of the longitudinal piezoelectric coefficient, d_{33}. This includes results on aging,[3] unipolar ac drive,[4] and high field ac bipolar drive.[4] The results during unipolar drive are the most promising, with little degradation witnessed in the piezoelectric response out to 10^9 cycles. Unfortunately, aging and bipolar degradation result in substantial losses in the longitudinal piezoelectric coefficient over time.

While the work on the longitudinal piezoelectric coefficient is illustrative, a majority of MEMS device structures require the transverse piezoelectric coefficient, d_{31}, for sensing and actuation. Consequently, this thesis focused on studying the factors that affect the stability of the d_{31} coefficient. Until recently, the transverse response was usually determined by resonance techniques on cantilever beams. The rigors of sample preparation and the complexity of both measuring and analyzing the data limit the usefulness of this technique. The recent development of the wafer flexure technique[5], however, facilitates monitoring d_{31} using a much simpler method.

Therefore, using the wafer flexure technique, an analysis of unipolar and bipolar drive reliability was performed to assess the lifetime of PZT thin film MEMS devices under electrical stress conditions. These experiments were designed to assist in determining the failure mechanisms responsible for piezoelectric degradation. In bulk actuators, results from the literature[6-8] point to electrode/ceramic delaminations, microcracking, and arc discharge as the most prominent failure mechanisms during ac cycling. In addition to these mechanisms, thin film piezoelectric device degradation may involve the influence of space charge and defect dipoles on depoling.[3, 4, 9] As well as examining ac reliability, experiments designed to determine the dc reliability of PZT thin films were conducted in a series of highly accelerated lifetime tests (HALT). These experiments enable a determination of the activation energy and voltage acceleration factor for failure. This thesis revolves around identifying the roles of each of the aforementioned failure mechanisms in PZT thin films with the explicit goals of providing a greater understanding of piezoelectric degradation and increasing reliability in PZT-based devices.

Chapter 2: Literature Survey

2.1 Introduction

This thesis focused on understanding the factors that determine the reliability of piezoelectric lead zirconate titanate thin film devices. This review describes the essential elements of ferroelectricity and piezoelectricity that recur throughout later chapters. In addition, a review of electromechanical degradation in bulk ceramics is presented in section 2.6 to describe possible mechanisms responsible for degradation in thin film devices.

2.2 Ferroelectric Materials

The identification of ferroelectric behavior in Rochelle salt in 1928 led to numerous research initiatives on this subject. Over the past 70 years, considerable progress has been made in topics such as phenomenology, the basis of ferroelectricity, and the development of useful devices. This review covers fundamental aspects of ferroelectricity.

A ferroelectric material is one in which a spontaneous electronic dipole moment can be re-oriented between crystallographically defined stable states by the application of an electric field. In the perovskite structure, ABO_3 (Figure 2.1), where A is a divalent ion and B is a tetravalent ion, a dipole moment develops as a result of a shift in the octahedrally coordinated tetravalent cation from the center of the unit cell. Additionally, the oxygen ions and A site ions may shift. For $Pb(Zr_xTi_{1-x})O_3$, the shift in position of the A-site, Pb^{+2} ions, also results in a contribution to the ferroelectric properties.

Consequently, a dipole moment is created between the center of negative charge and the center of positive charge.

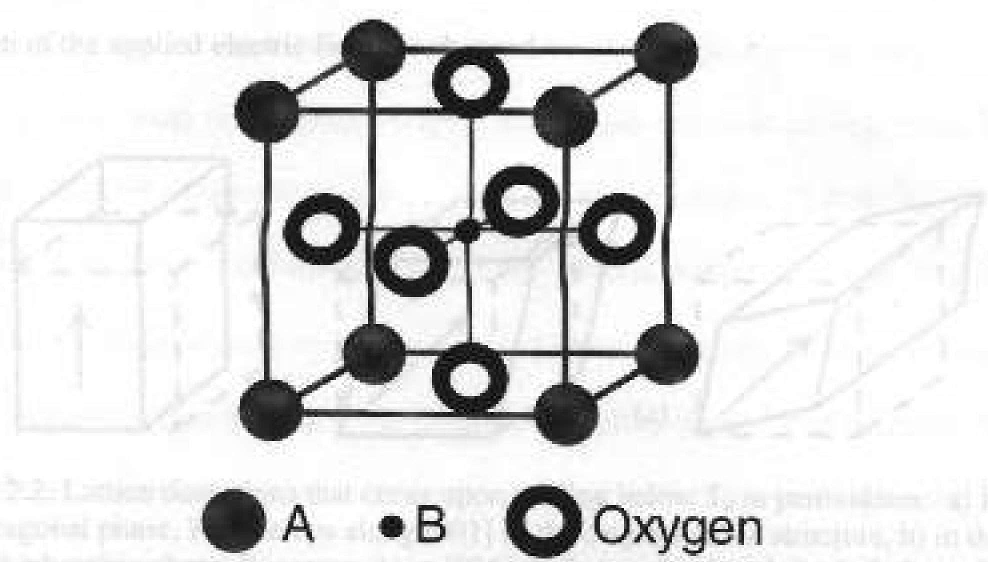

Figure 2.1: Representation of the cubic (Pm3m) prototype structure of perovskite ABO_3 structure.

In perovskites, the development of the dipole occurs at a phase transition from a non-polar paraelectric state to a polar ferroelectric state. This transition at the Curie temperature (T_c) is associated with a structural change from a centrosymmetric cubic phase to a non-centrosymmetric distorted phase. Additional transitions temperatures can exist between two non-centrosymmetric distorted phases (i.e. tetragonal to orthorhombic or orthorhombic to rhombohedral). Figure 2.2 illustrates the lattice distortions that yield the observed structural changes in barium titanate ($BaTiO_3$). A tetragonal structure results through expansion of the unit cell in the [001] direction, while an expansion along the [111] direction results in a rhombohedral structure.

The development of a dipole at T_c creates a spontaneous polarization in each unit cell of the material. This polarization can be permanently re-oriented into different

equilibrium states with an applied electric field, leading to the most recognizable aspect of ferroelectricity: the polarization electric field hysteresis loop (see Figure 2.3). This loop results from the change in net polarization of the material as the amplitude and direction of the applied electric field are changed.

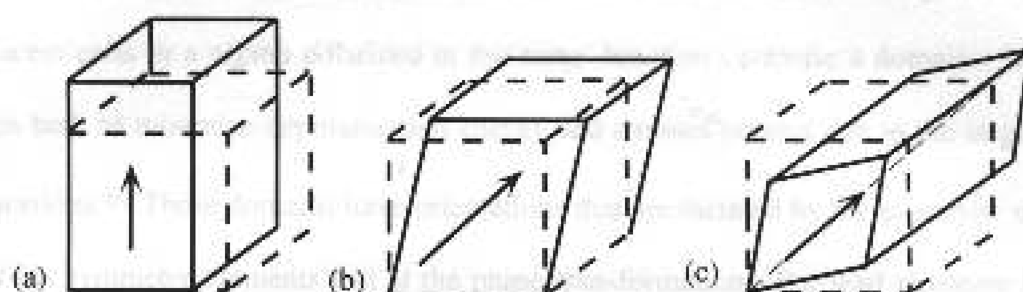

Figure 2.2: Lattice distortions that occur upon cooling below T_c in perovskites: a) In the tetragonal phase, P_s develops along [001] of the original cubic structure, b) in the orthorhombic phase, P_s occurs along [011], and c) in the rhombohedral phase, P_s develops along [111]. The dotted cubes are for the cubic prototype; the solid lines show the distorted unit cells of the ferroelectric phases.

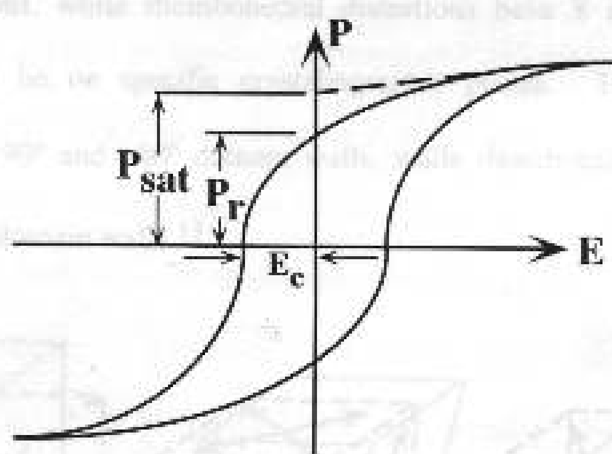

Figure 2.3: Schematic of the polarization electric field hysteresis loop illustrating the saturation polarization (P_{sat}), remanent polarization (P_r), and coercive field (E_c).

The saturation polarization, P_{sat}, is defined as the linear extrapolation of the high field polarization to zero field and represents the maximal amount of dipole alignment

achieved at a given electric field. The remanent polarization, P_r, is the retained polarization at zero electric field. The coercive field, E_c, is the field, which results in a net zero polarization. The polarization electric field hysteresis loop is a fundamental aspect of ferroelectricity and illustrates the reorientability of the dipole moment.

A spontaneous polarization develops in each unit cell upon cooling below T_c. All adjacent cells in a region polarized in the same direction comprise a domain. Domains form both to minimize depolarization energy and stresses present due to the large lattice distortions.[10] These domains have orientations that are dictated by the prototype unit cell and the symmetry elements lost at the phase transformation. For lead zirconate titanate (PZT), which can possess either a tetragonal or rhombohedral unit cell depending on the Zr:Ti ratio, the polarization direction is along the original <001> or <111> axes of the cubic prototype (see Figure 2.4). Tetragonally distorted PZT possesses 6 equivalent polarization directions, while rhombohedral distortions have 8 equivalent directions. Domain boundaries lie on specific crystallographic planes. Tetragonally distorted perovskites possess 90° and 180° domain walls, while rhombohedral perovskites have 71°, 109°, and 180° domain walls.[11]

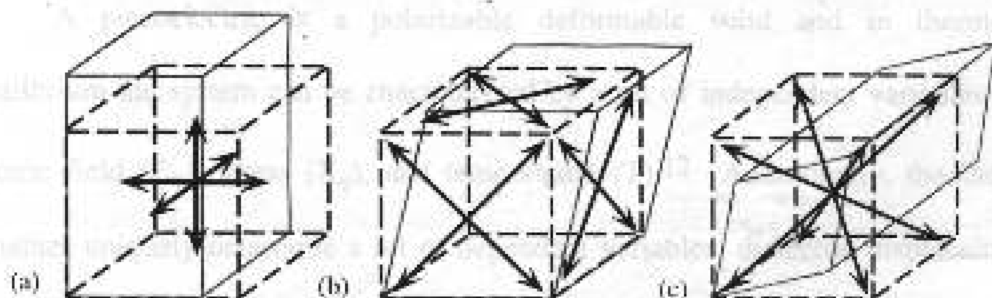

Figure 2.4: Possible polarization directions relative to the cubic prototype for a) tetragonal perovskite with 6 equivalent <001> directions, b) orthorhombic distortion with 12 equivalent <110> directions, or c) rhombohedral with 8 equivalent <111> directions.

A ferroelectric also possesses a very high relative permittivity (ε_r) or dielectric constant (K). Nominally, the dielectric constant is the ratio of the material permittivity (ε) to the permittivity of free space (ε_o).

$$\varepsilon_r = k = \frac{\varepsilon}{\varepsilon_0}. \tag{2.1}$$

Under ac electrical fields, the dielectric constant can be described as a complex number with an in phase and out of phase component with respect to the applied voltage. The out of phase component is primarily due to dielectric absorption, resistive leakage, and domain wall motion. The dielectric loss, represented as D or tan δ, is the ratio of the out of phase and in phase components.[11] The dielectric constant and dielectric loss are very important parameters for determining a material's usefulness as a capacitor.

2.2.1 Phenomenology

Many of the physical properties of ferroelectric materials can be described via phenomenology.[12] The review here will be brief and is intended to provide knowledge on topics that will be discussed in later chapters. The descriptions generated by phenomenology are strictly valid for single domain specimens.

A piezoelectric is a polarizable deformable solid and in thermodynamic equilibrium the system can be characterized by a set of independent variables including electric field (E_m), stress (X_{ij}), and temperature (T).[12] Additionally, the independent variables uniquely determine a set of dependent variables: dielectric displacement (D_m), strain (x_{ij}), and entropy. In the descriptions following, dielectric displacement is replaced by polarization (P_m) through the following relation:

$$P_m = D_m - \varepsilon_0 E_m \, . \qquad (2.1)$$

Using the set of independent and dependent variables, a set of thermodynamic potentials (see Table 2.1) develop. These potentials can be used to describe many of the basic material properties by taking the partial derivatives of the thermodynamic potentials. This provides a description of the material properties.

Table 2.1: Thermodynamic potentials for a polarizable deformable solid with the boundary conditions for each potential. The independent variables are temperature (T), stress (X_{ij}), and electric field (E_m) while the dependent variables are polarization (P_m), strain (x_{ij}), and entropy (S).[12]

Thermodynamic Potentials		Boundary Conditions
Helmholtz Free Energy	$\delta A = -S\delta T - X_{ij}\delta x_{ij} + E_m \delta P_m$	T x P
Enthalpy	$\delta H = T\delta S + x_{ij}\delta X_{ij} - P_m \delta E_m$	S X E
Elastic Enthalpy	$\delta H_1 = T\delta S + x_{ij}\delta X_{ij} + E_m \delta P_m$	S X P
Electric Enthalpy	$\delta H_2 = T\delta S - X_{ij}\delta x_{ij} - P_m \delta E_m$	S x E
Full Gibbs Free Energy	$\delta G = -S\delta T + x_{ij}\delta X_{ij} - P_m \delta E_m$	T X E
Elastic Gibbs Free Energy	$\delta G_1 = -S\delta T + x_{ij}\delta X_{ij} + E_m \delta P_m$	T X P
Electric Gibbs Free Energy	$\delta G_2 = -S\delta T - X_{ij}\delta x_{ij} - P_m \delta E_m$	T x E
Internal Energy	$\delta U = T\delta S - X_{ij}\delta x_{ij} + E_m \delta P_m$	S x P

Reviewing the Helmholtz free energy, the following Maxwellian relations result:

$$-S = \left(\frac{\delta A}{\delta T}\right)_{xP}, \quad X_{ij} = \left(\frac{\delta A}{\delta x_{ij}}\right)_{TP}, \quad E_m = \left(\frac{\delta A}{\delta P_m}\right)_{Tx}. \qquad (2.2)$$

Taking the second partial derivatives leads to a phenomenological depiction of material parameters. Again with the Helmholtz equation, the following relationships are developed:[12]

$$\left(\frac{\delta^2 A}{\delta T^2}\right)_{xP} = -\left(\frac{\delta S}{\delta T}\right)_{xP} = -\frac{c_{x_{ij}P_m}}{T} \quad \text{specific heat,} \quad (2.3)$$

$$\left(\frac{\delta^2 A}{\delta x_{ij}^{\ 2}}\right)_{TP} = \left(\frac{\delta X_{ij}}{\delta x_{kl}}\right)_{TP} = c_{ijkl} \quad \text{elastic constant.} \quad (2.4)$$

$$\left(\frac{\delta^2 A}{\delta P_m^{\ 2}}\right)_{xT} = \left(\frac{\delta E_m}{\delta P_m}\right)_{xT} = \chi \quad \text{dielectric reciprocal susceptibility.} \quad (2.5)$$

In addition to these direct relationships relating E and P, X and x, and T and S, mixed relationships can be generated by taking the second partial with respect to one of the remaining boundary variables. The relations focused on in this thesis will involve those relating electromechanical properties (i.e. relating E and P to X and x). Again starting with the Helmholtz free energy the following electromechanical relationships develop:[12]

$$\left(\frac{\delta^2 A}{\delta P_m \delta x_{ij}}\right)_T = -\left(\frac{\delta X_{ij}}{\delta P_m}\right)_{xT}, \quad (2.6)$$

$$\left(\frac{\delta^2 A}{\delta x_{ij} \delta P_m}\right)_T = \left(\frac{\delta E_m}{\delta x_{ij}}\right)_{PT}. \quad (2.7)$$

Equations 2.5 and 2.6 are equal so that ,

$$\left(\frac{\delta^2 A}{\delta P_m \delta x_{ij}}\right)_T = -\left(\frac{\delta X_{ij}}{\delta P_m}\right)_{xT} = \left(\frac{\delta E_m}{\delta x_{ij}}\right)_{PT} = h_{mij}, \quad (2.8)$$

where h_{mij} is one of the 4 piezoelectric coefficients. The other piezoelectric coefficients are derived from the remaining thermodynamic potentials in a similar manner and are located in Table 2.2. This thesis will focus on the d_{mij} coefficients relating P_m and X_{ij} at constant field and E_m and x_{ij} at constant stress.

The application of an electric field to a piezoelectric material produces a strain directly proportional to the field. Additionally, there is a strain generated that is proportional to the square of the field (or more appropriately, the square of the polarization. This second order effect is known as electrostriction and occurs in all materials. Just as there are 4 piezoelectric coefficients, there are 4 electrostrictive coefficients. However, for the purpose of this investigation the focus will remain on the Q_{ijmn} term defined as:[12]

$$x_{ij} = -s_{ij}^{P} X_{ij} + Q_{ijmn} P_m P_n \qquad (2.9)$$

$$2Q_{ijmn} = \frac{\delta^2 E_m}{\delta X_{ij} \delta P_n} \qquad (2.10)$$

The first partial derivative with respect to P_m in equation 2.8 yields the following relationship:

$$\left(\frac{dx_{ij}}{dP_m}\right)_X = 2Q_{ijmn} P_n = h_{mij} \qquad (2.11)$$

Thus, the piezoelectric effect in a ferroelectric can be related to the electrostrictive response biased by the polarization.

Table 2.2: Thermodynamically derived definitions of the four piezoelectric coefficients: d_{mij}, g_{mij}, e_{mij}, h_{mij}.[12]

$\left(\frac{\delta^2 A}{\delta P_m \delta x_{ij}}\right)_T = -\left(\frac{\delta X_{ij}}{\delta P_m}\right)_{xT} = -\left(\frac{\delta E_m}{\delta x_{ij}}\right)_{PT} = h_{mij}$	$\left(\frac{\delta^2 H}{\delta E_m \delta X_{ij}}\right)_S = -\left(\frac{\delta x_{ij}}{\delta E_m}\right)_{SX} = \left(\frac{\delta P_m}{\delta X_{ij}}\right)_{SE} = d_{mij}$
$\left(\frac{\delta^2 H_1}{\delta P_m \delta X_{ij}}\right)_S = -\left(\frac{\delta x_{ij}}{\delta P_m}\right)_{SX} = \left(\frac{\delta E_m}{\delta X_{ij}}\right)_{SP} = g_{mij}$	$\left(\frac{\delta^2 H_2}{\delta E_m \delta x_{ij}}\right)_S = -\left(\frac{\delta X_{ij}}{\delta E_m}\right)_{Sx} = -\left(\frac{\delta P_m}{\delta x_{ij}}\right)_{SE} = e_{mij}$
$\left(\frac{\delta^2 G}{\delta X_{ij} \delta E_m}\right)_T = -\left(\frac{\delta P_m}{\delta X_{ij}}\right)_{TE} = -\left(\frac{\delta x_{ij}}{\delta E_m}\right)_{TX} = d_{mij}$	$\left(\frac{\delta^2 G_1}{\delta P_m \delta X_{ij}}\right)_T = -\left(\frac{\delta x_{ij}}{\delta P_m}\right)_{TX} = \left(\frac{\delta E_m}{\delta X_{ij}}\right)_{TP} = g_{mij}$
$\left(\frac{\delta^2 G_2}{\delta E_m \delta x_{ij}}\right)_T = -\left(\frac{\delta X_{ij}}{\delta E_m}\right)_{Tx} = \left(\frac{\delta P_m}{\delta x_{ij}}\right)_{TE} = e_{mij}$	$\left(\frac{\delta^2 U}{\delta P_m \delta x_{ij}}\right)_S = -\left(\frac{\delta X_{ij}}{\delta P_m}\right)_{Sx} = \left(\frac{\delta E_m}{\delta x_{ij}}\right)_{SP} = h_{mij}$

2.3 Lead Zirconate Titanate (PZT)

Most solid solutions between $PbZrO_3$ and $PbTiO_3$ possess ferroelectricity and show excellent piezoelectric properties. By varying the Zr^{+4}/Ti^{+4} ratio, both the ferroelectric and piezoelectric properties can be altered significantly.

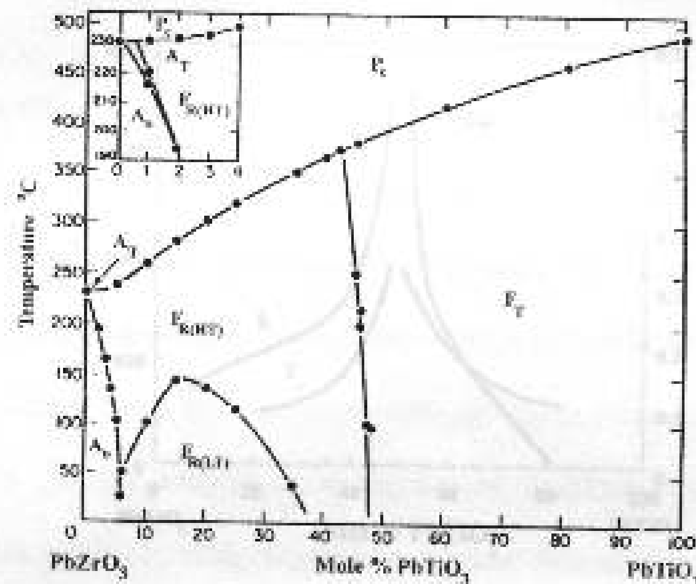

Figure 2.5: Phase diagram for the lead zirconate - lead titanate solid solution.[13]

The phase diagram in Figure 2.5 illustrates the structural changes that occur as a result of composition variations. Substitutions of Zr^{+4} for Ti^{+4} in $PbTiO_3$ reduce the tetragonal distortion and cause the structure to become rhombohedral.[10] As seen in the phase diagram, the shift from a tetragonal to a rhombohedral structure occurs at a morphotropic phase boundary (MPB) near the Zr^{+4}/Ti^{+4} ratio of 52/48. A MPB denotes an abrupt structure change with composition at a constant temperature.[11] From phase equilibrium the MPB is required to be a two-phase mixture of the tetragonal and rhombohedral structures. The presence of both of these structures in this region gives the material an increased number of polarization directions. For MPB compositions,

polarization directions include both the prototype <100> and <111> directions and result in extremely large dielectric and piezoelectric properties, as seen in Figure 2.6. The presence of such large piezoelectric properties near the MPB make PZT an extremely attractive candidate for piezoelectric devices.

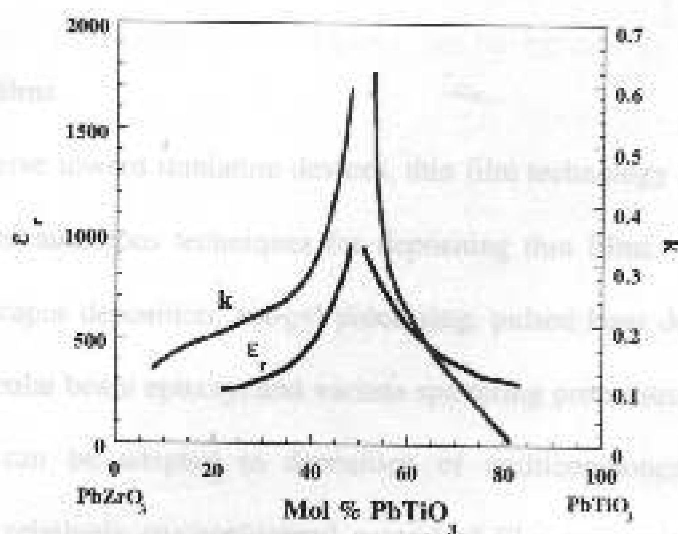

Figure 2.6: Variation in relative permittivity and piezoelectric coupling coefficient (k) with variation in the Zr/Ti ratio for PZT ceramics.[11]

2.3.1 Hard and Soft PZT Ceramics

In many cases, PZT ceramics are deliberately doped to control both the ferroelectric and piezoelectric properties of the ceramics. Substitutions of higher valent ions, donors, such as Nb^{+5} or Ta^{+5} to replace Ti^{+4} and La^{+3} to replace Pb^{+2}, result in the creation of Pb vacancies (V_{Pb}'') to compensate for the increase in charge of the matrix. These vacancies are associated with "soft" PZT, which show small coercive fields and aging rates, but larger dielectric constants, dielectric losses, and piezoelectric coefficients.[11] On the other hand, additions of lower valent ions, acceptors, such as Mg^{+2} or Fe^{+3} for Ti^{+4} generate positive oxygen vacancies ($V_O^{\bullet\bullet}$) as charge compensation and

lead to "hard" PZT. These compositions possess lower dielectric constants, low dielectric loss, large coercive fields, smaller piezoelectric coefficients, and faster aging rates.[11] The differences in the piezoelectric coefficients for hard and soft PZT is largely attributed to the ease of domain wall motion, resulting in larger d-coefficients for soft PZT.

2.3.2 PZT Thin Films

With the drive toward miniature devices, thin film technology has exploded with the development of numerous techniques for depositing thin films. These techniques include chemical vapor deposition, sol-gel processing, pulsed laser deposition, reactive evaporation, molecular beam epitaxy, and various sputtering procedures. While many of these techniques can be adapted to deposition of multicomponent oxides, sol-gel processing allows relatively straightforward control of film composition. Sol-gel spin coating enables homogeneous coating over large areas and is easy and cheaper than most methods because it does not require the use of expensive vacuum equipment.

It has been demonstrated by several groups that PZT thin films possess smaller piezoelectric coefficients than bulk ceramics.[5, 14, 15] One reason for the large deviation from bulk ceramics is clamping of the film to the substrate. The substrate prohibits the film from expanding or contracting freely in the plane, reducing the amount of observed mechanical strain.[16] Another factor reducing the extrinsic response may be the limited number or mobility of non-180° domain walls, which can contribute ~50% to the bulk piezoelectric coefficients (see section 2.4.2).[17-19]

The response of films to doping can also differ from that in bulk ceramics. Bulk PZT's are often donor-doped to facilitate domain wall motion. Since this wall motion dominates the dielectric loss, tan d increases with donor doping. In contrast, films often have much higher electronic conductivities and lower domain wall mobilities than bulk ceramics. Thus, donor doping in films results in a decrease in the dielectric loss and the leakage current for small dopant concentrations, not an increase as occurs with donor doping of ceramics.[20, 21]

2.4 Piezoelectricity

All insulating materials exhibit a dimensional change when subjected to an applied electric field.[11] There are two different mechanisms responsible for the dimensional change. If the strain generated is proportional to the square of the electric field then the strain is generated by the electrostrictive response. On the other hand, if the strain is directly proportional to the electric field, then the piezoelectric effect is the responsible mechanism for the shape change. In addition, piezoelectric materials develop an electric charge upon the application of a stress.[10] These effects are utilized in a wide range of devices including actuators, transducers, and sensor arrays.

2.4.1 Direct and Converse Piezoelectric Effect

The direct and converse piezoelectric effects are each illustrated in Figure 2.7. The direct piezoelectric effect relates the induced polarization, P_m, to the applied stress, X_{ij}, and is described by the following equation:

$$P_m = \left(\frac{Q}{A}\right) = d_{mij} X_{ij}, \quad (2.12)$$

where Q is charge, A is area, and d_{mij} is the piezoelectric coefficient expressed in Coulombs/Newton. Conversely, an electric field, E_m, can generate a strain, x_{ij}, in the material:

$$x_{ij} = d_{mij} E_m , \qquad (2.13)$$

with the d-coefficients expressed in meters/volt.

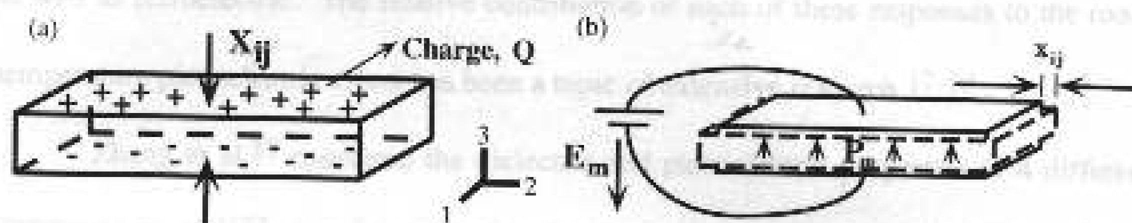

Figure 2.7: The direct and converse piezoelectric effects. (a) The direct effect is the generation of a surface charge, Q, upon the application of an applied stress, X. In this depiction, the d_{333} coefficient is presented with the stress applied on the 1-2 plane in the 3 direction and the generated charge accumulates along the 3 direction. (b) The converse effect is the dimensional change of the material, or strain, x, upon the application of an electric field. This schematic illustrates both a contraction along the 3 direction using d_{333} and expansions in the 1 and 2 directions by d_{311} and d_{322}.

A majority of piezoelectric devices utilize the longitudinal piezoelectric coefficient, d_{333}, or the transverse piezoelectric coefficient, d_{311}. By convention, the two subscripts associated with the stress and strain (i and j) are reduced to one (i) by describing the orthogonal stresses or strains as the numbers 1 – 3 and the shear components as 4 – 6.[22] Thus, the d_{333} and d_{311} coefficients described in Figure 2.7 are given in contracted notation as d_{33} and d_{31}, respectively. This thesis will focus on the transverse piezoelectric coefficient, d_{31}.

2.4.2 Intrinsic and Extrinsic Contribution to the Piezoelectric Effect

Piezoelectricity is comprised of two contributions, intrinsic and extrinsic. The intrinsic response is from the expansion and contraction of the crystal lattice due to the applied field, whereas the extrinsic contribution results largely from motion of ferroelastic domains.[13] Non-180° domain walls separate domains which are ferroelastic as well as ferroelectric. The relative contribution of each of these responses to the room temperature piezoelectric effect has been a topic of extensive research.[17-19]

Zhang et al.[17] measured the dielectric and piezoelectric properties of 4 different compositions of PZT as a function of temperature from 4 to 300K. The compositions were MPB PZT doped with NiO (Type 1), Nb_2O_5 (Type 2), Fe_2O_3 (Type 3), and Sb_2O_5 (Type 4). Figure 2.8 illustrates that although K and d_{31} are different at room temperature for the 4 compositions, all compositions converge to the same K and d_{31} values at 4K. Since domain wall motion is a thermally activated process, it is eliminated at lower temperatures. Thus, the large differences at room temperature in the dielectric and piezoelectric properties can be attributed to extrinsic contributions. Therefore, the extrinsic response comprised up to 60% of the room temperature piezoelectric values for soft PZT.

Other work quantifying the relative contributions of the two responses to the room temperature piezoelectric effect has been reported by Zhang et al.[18] and Damjanovic et al.[19] Zhang monitored the hydrostatic (d_h), longitudinal, and transverse piezoelectric coefficients versus temperature. They assumed that d_h resulting solely from intrinsic responses, since the polarization change from domain wall motion does not involve a volume change. On the other hand, d_{33} and d_{31} result from both intrinsic and extrinsic

responses. Their results revealed that d_h was approximately constant over the observed temperature range of 10 to 300K while d_{33} and d_{31} exhibited substantial increases with temperature. The difference was attributed to large extrinsic contributions for the longitudinal and transverse piezoelectric coefficients.

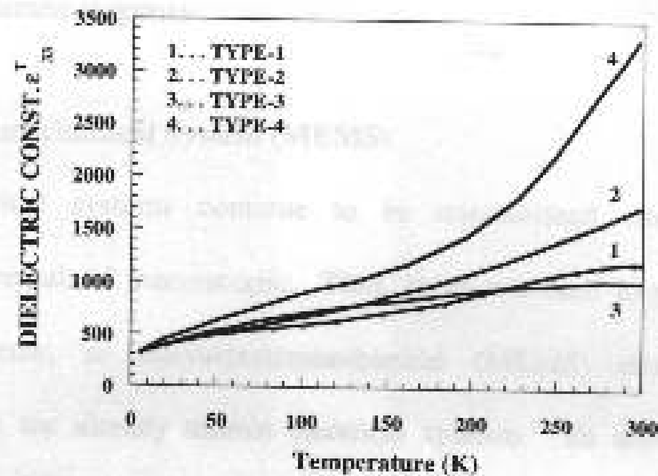

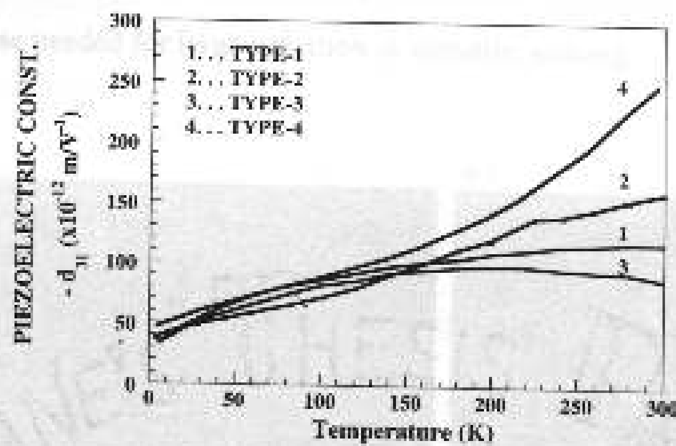

Figure 2.8: Temperature dependence of the dielectric constant and transverse piezoelectric coefficient for 4 different bulk compositions of PZT. Types 1 and 3 are hard PZTs doped with NiO and Fe_2O_3, respectively. Types 2 and 4 are soft PZT doped with Nb_2O_5 and Sb_2O_3, respectively.[17]

Recently, Damjanovic et al.[19] have shown that in PZT ceramics irreversible domain wall motion provides a significant contribution to the piezoelectric response. They measured the piezoelectric response as a function of applied stress amplitude. Then, the contribution from extrinsic effects was calculated using the Raleigh Law. They concluded that irreversible domain wall motion contributes between 20 and 40% of the measured piezoelectric response.

2.5 Microelectromechanical System (MEMS)

As electrical systems continue to be miniaturized, mechanical parts and equipment have remained macroscopic. Thus, there is a need to produce miniaturized mechanical systems, or microelectromechanical (MEMS) devices, that can be incorporated with the already minute electrical systems. To accomplish this goal, a piezoelectric material is required with large d-coefficients which can produce the strain or electrical response needed for large actuation or sensitive sensing.

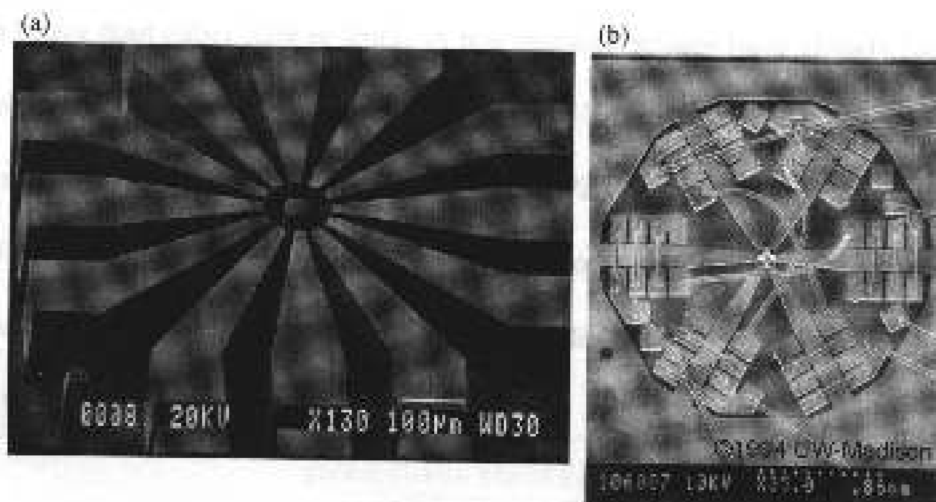

Figure 2.9: Scanning electron micrographs of a) a micro slide motor constructed of polysilicon and b) a micro motor constructed of permalloy.[23, 24]

2.5.1 Thin Film MEMS Devices

Many piezoelectric MEMS devices have been fabricated using AlN and ZnO. Devices (see Figure 2.9) including micromotors, accelerometers, and microgears, have all been fabricated using established Si processing routes. However, AlN and ZnO are only able to achieve small strains due to their relatively small d-coefficients. Thus, there is a desire to switch to a material that has much larger piezoelectric constants.

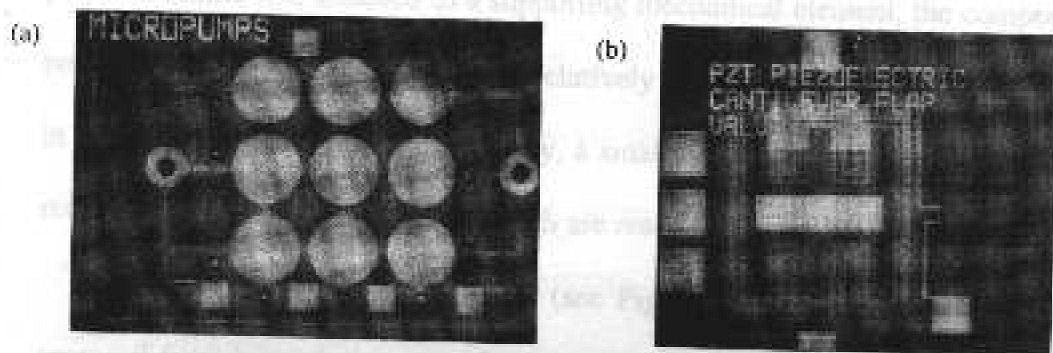

Figure 2.10: Scanning electron micrographs of a) a micropump and b) a microvalve using PZT thin films as the actuator.[1]

PZT is very attractive as the replacement material, with d-coefficients an order of magnitude larger than either AlN or ZnO. A few research groups have already fabricated devices using PZT as the active material. Figure 2.10 illustrates the feasibility of manufacturing micropumps and microvalves using PZT. The micropump featured in Figure 2.10a uses a PZT diaphragm structure to transport a medium between 2 ports. On the other hand, the device in Figure 2.10b uses a cantilever beam design to open or close a microvalve.

2.5.2 MEMS Design

To create actuation with piezoelectric materials, most MEMS utilize the transverse piezoelectric response. This is a direct result of the limited displacement that can be achieved longitudinally in films. To increase the available displacements, mechanical amplifiers such as cantilevers and diaphragms are used. When a piezoelectric film on a supporting structure is electrically excited, it attempts to expand or contract in plane. Because it is attached to a supporting mechanical element, the composite element bends in the out of plane direction. Relatively small piezoelectric strains can thus result in more substantial motions. Similarly, a small normal stress can bend such a member, resulting in large in-plane strains, which are readily detected piezoelectrically.

In the cantilever beam design (see Figure 2.11a), a portion of the substrate is removed from beneath the piezoelectric material. In addition, material from three sides of the beam is removed. The strains produced by the transverse piezoelectric response flex the beam up or down depending on the direction of the applied electric field and the direction of the polarization.

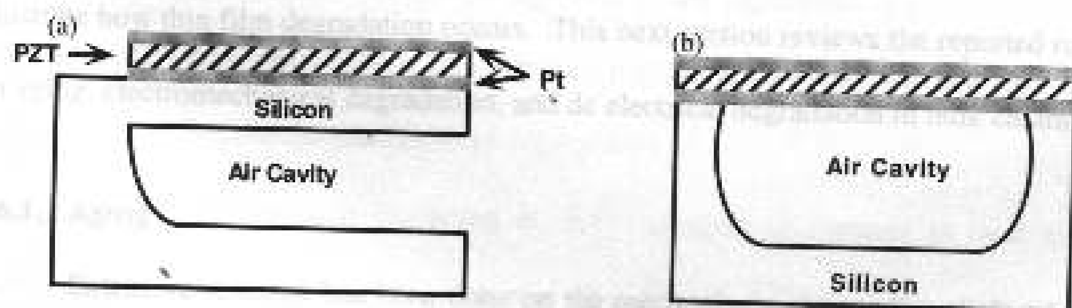

Figure 2.11: Schematic of a) a cantilever beam and b) a diaphragm design for piezoelectric MEMS devices.

In a diaphragm design (see Figure 2.11b), the substrate beneath the ferroelectric thin film is removed. This cavity can be filled with either gases or liquids. The actuator

material is rigidly attached to the substrate near the edges of the diaphragm. Similar to the beam design, the transverse piezoelectric response causes the structure to flex up or down, resulting in expansion or contraction of the air cavity. Sequentially opening and closing a series of diaphragm structures connected by ports creates a micropump similar to Figure 2.10a.

2.6 Degradation Mechanisms

Piezoelectric actuators are widely used in numerous applications.[8] In many bulk ceramic actuators, the drive conditions are deliberately limited to minimize premature failure of the device. Piezoelectric aging, mechanical failure at field or stress concentrations, electromechanical degradation, and dc electric fields can all lead to failure in bulk actuators. In thin film actuators, the factors that limit the reliability are not well understood.

2.6.1 Bulk Ceramics

Examining the mechanisms affecting reliability in bulk ceramics may help illustrate how thin film degradation occurs. This next section reviews the reported results on aging, electromechanical degradation, and dc electrical degradation in bulk ceramics.

2.6.1.1 Aging

Extensive research has been done on the mechanisms surrounding dielectric and piezoelectric aging. Aging is the gradual decrease in the dielectric or piezoelectric responses with time in the absence of mechanical, electrical, or temperature stress changes. Aging rates of a few percent per decade are typical for most piezoelectric

ceramics.[11] In bulk ceramics, the aging of K and d_{33} occur at approximately the same rates.[3] The aging of K and d_{33} appear to be related to a reduction in domain wall mobility.[25, 26] Over time, the domain walls become pinned by the creation of space charge or internal stress, thus reducing the extrinsic contributions to the dielectric and piezoelectric response.

2.6.1.2 Electromechanical Degradation

Electromechanical degradation, or the loss of the piezoelectric response after repeated electric field cycles, is critical for determining actuator reliability. Both unipolar and bipolar electric field stresses affect reliability. These stresses simulate operating conditions and suggest how the device will operate under extreme conditions.

Experiments by Wang et al.[27] on $PbZr_{0.53}Ti_{0.47}O_3$ (PZT-5H) centered on determining the mechanisms behind polarization fatigue and electromechanical degradation. Applying a bipolar electric field of varying magnitudes, they monitored the polarization, permittivity, and transverse piezoelectric parameters over time. Their results (presented in Figure 2.12) reveal that each of the parameters is severely degraded after only 10^6 cycles for fields of 20 kV/cm or higher. It is also noted that each of the parameters exhibits similar electric field dependence.

Unipolar experiments by Wang et al.[27] revealed, in contrast to their bipolar results, very stable piezoelectric properties (see Figure 2.13). Their results exhibit minimal loss in d_{31} when cycled from 0 – 80 kV/cm and d_{31} actually increases with cycling for asymmetric fields of -8.5 – 40 kV/cm. The difference between these two

results is thought to be a result of an increase in either domain wall concentration or mobility as the poling state is altered by the asymmetric electric field.

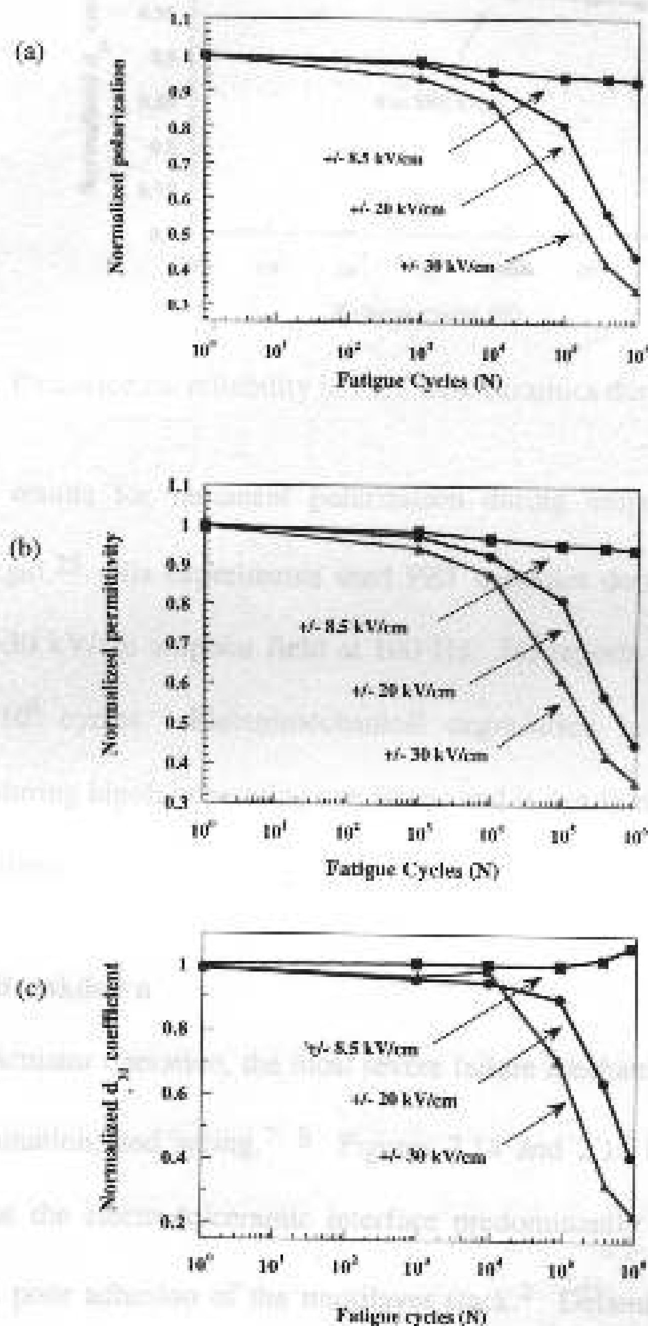

Figure 2.12: Degradation of a) switchable polarization, b) permittivity, and c) transverse piezoelectric coefficient as a function of bipolar electrical cycles in PZT bulk ceramics. Fatigue degradation occurs in each property and the same electric field dependence is witnessed for each property.[27]

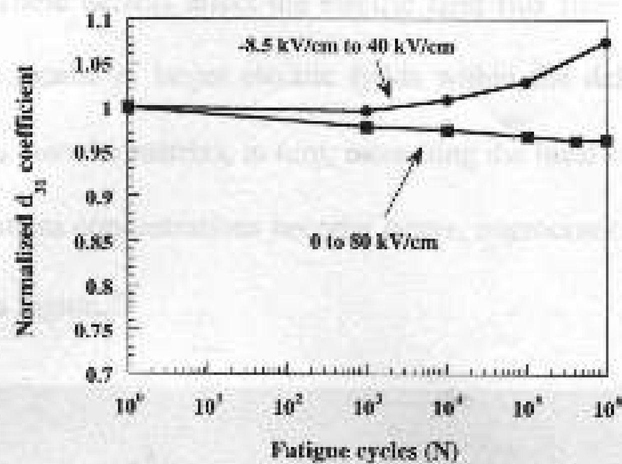

Figure 2.13: Piezoelectric reliability in PZT bulk ceramics during unipolar drive.[27]

Similar results for remanent polarization during unipolar fatigue have been obtained by Ozgul.[28] His experiments used PZT ceramics doped with 2 wt% Nb and driven with a ~30 kV/cm unipolar field at 100 Hz. He reports near stable polarization values up to 10^6 cycles. Electromechanical degradation in bulk ceramics occurs predominantly during bipolar operating conditions and is nearly non-existent for unipolar operating conditions

2.6.1.3 Device Breakdown

During actuator operation, the most severe failure mechanisms are microcracking, electrode delamination, and arcing.[7, 8] Figures 2.14 and 2.15 illustrate these failures. Delaminations at the electrode/ceramic interface predominantly result from processing defects, such as poor adhesion of the multilayer stack.[7] Delamination results in lower dielectric and piezoelectric values and more severely increased electrical stresses. Microcracking, similar to delaminations, can be a result of processing defects. Voids, pores, edges of internal electrodes, and grain boundaries are sites for microcrack

initiation.[7, 29-31] These defects affect the electric field flux lines in their vicinity (see Figure 2.16). This results in larger electric fields within the defect region (since the defect has a lower ε_r than the matrix), in turn, increasing the local strain in the vicinity of the defect. As the stress concentrations become larger, microcracks develop to relax the elastic energy in this region.[32]

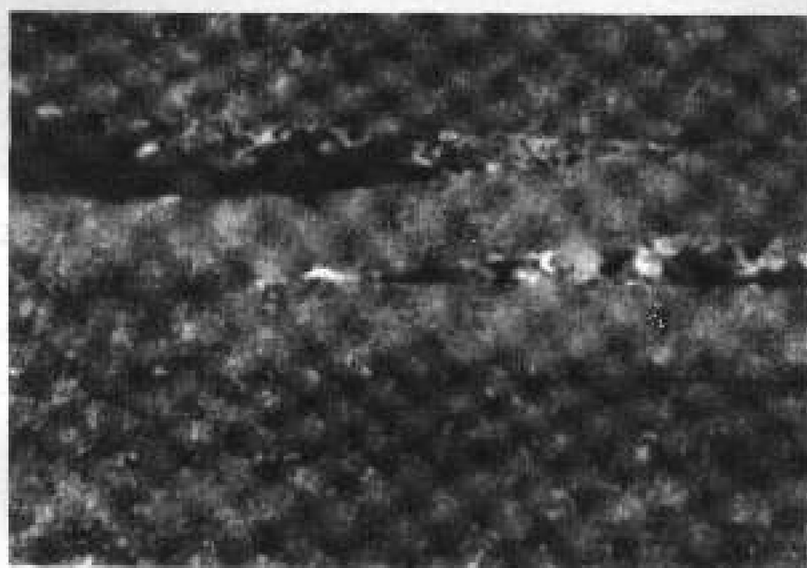

Figure 2.14: Delamination at the electrode ceramic interface in a multilayer actuator.[7]

An additional failure mechanism in multilayer actuators is gas discharge breakdown or arcing. Arcing occurs at extremely large electric fields (~1MV/m) and is the result of an electronic discharge between electrodes.[7] As shown in Figure 2.17, this type of failure is extremely destructive. A majority of arcing events result from processing defects, especially pores and voids near electrodes.[7] These defects provide cavities which as shown in Figure 2.16 can increase the local electric field. The larger electric field within this cavity appears to be the starting point for a discharge event.[11]

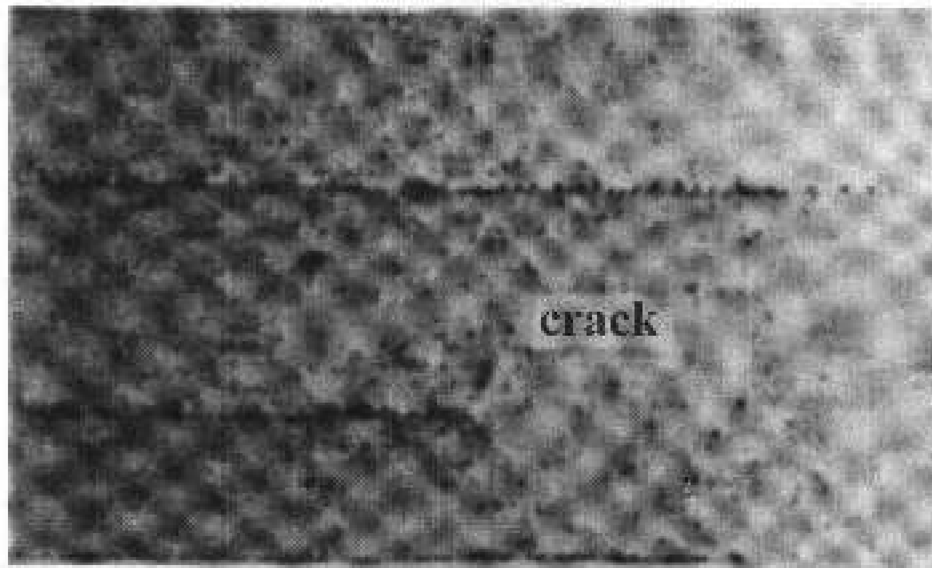

Figure 2.15: Microcrack initiation at the termination of an internal electrode of a multilayer actuator.[6]

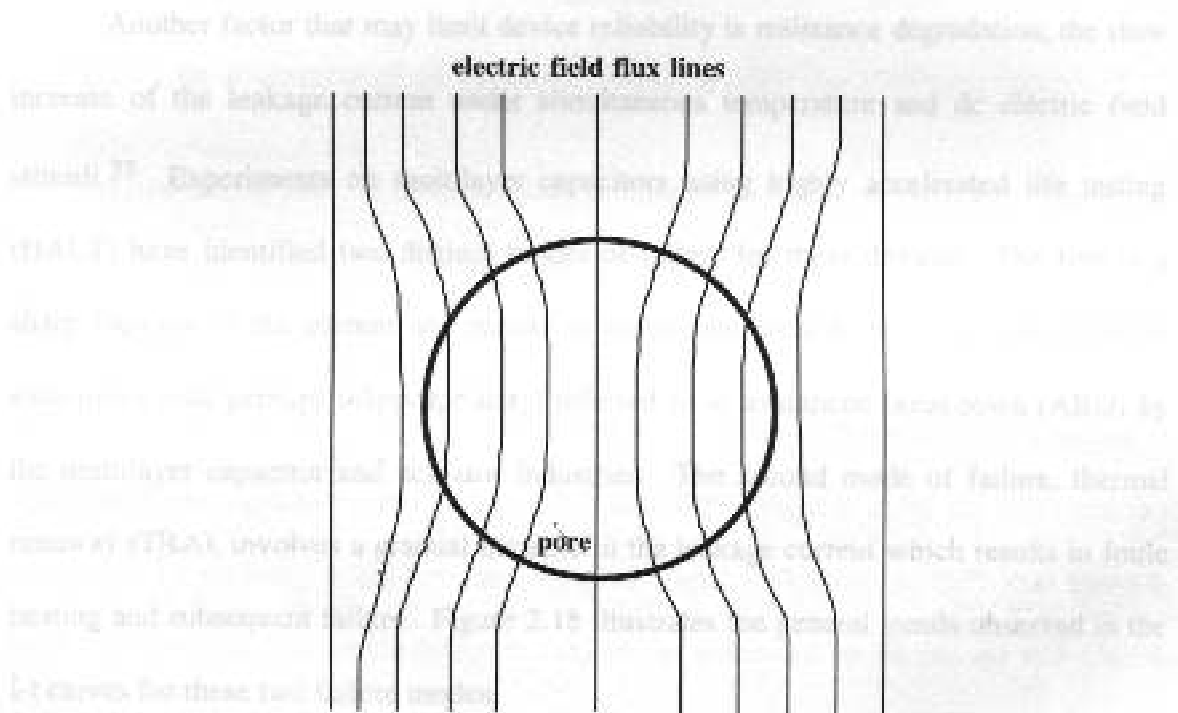

Figure 2.16: Schematic of electric field impingement in the vicinity of a pore.

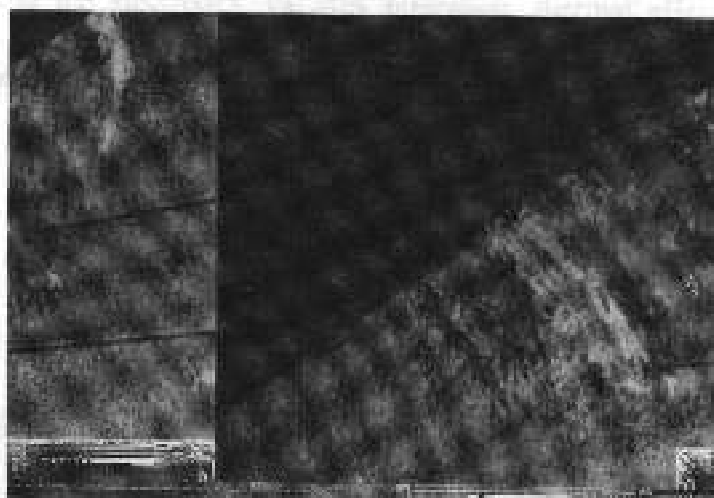

Figure 2.17: Remanents of an arcing discharge illustrating a void as the catalyst for failure.[7]

Another factor that may limit device reliability is resistance degradation, the slow increase of the leakage current under simultaneous temperature and dc electric field stimuli.[33] Experiments on multilayer capacitors using highly accelerated life testing (HALT) have identified two distinct modes of failure for these devices. The first is a sharp increase in the current and results in immediate breakdown. This fast failure is sometimes (and perhaps inappropriately) referred to as avalanche breakdown (ABD) by the multilayer capacitor and actuator industries. The second mode of failure, thermal runaway (TRA), involves a gradual increase in the leakage current which results in Joule heating and subsequent failure. Figure 2.18 illustrates the general trends observed in the I-t curves for these two failure modes.

The mechanisms responsible for ABD failures are extrinsic in nature and encompass porosity, processing defects, and microcracks.[34] On the other hand, TRA type failures generally occur from intrinsic mechanisms including electrochemical

reactions at the electrodes, vacancy migration, thermal effects, and catastrophic ion-impact ionization.[34]

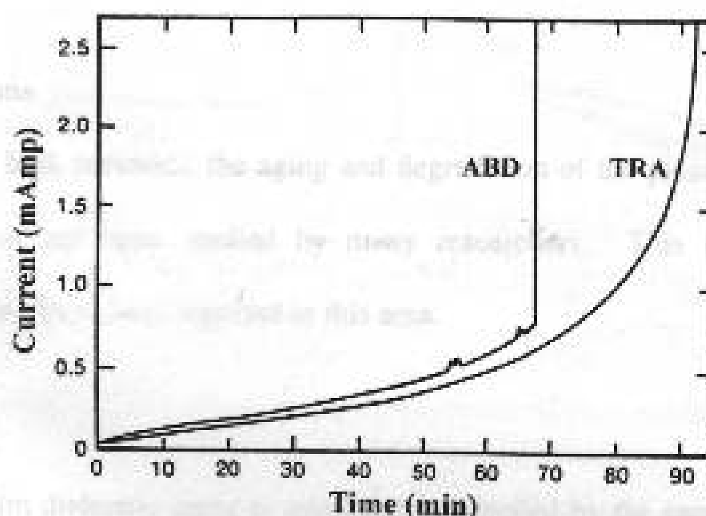

Figure 2.18: Illustration of the I-t curves typical for ABD and TRA type failures.[35]

Experiments with dc fields on bulk perovskite ceramics revealed that breakdown of the insulation resistance primarily results from $V_O^{\bullet\bullet}$ migration.[36-38] Under these applied fields and elevated temperatures, $V_O^{\bullet\bullet}$ migrate towards the anode. Waser et al.'s[36] electrocoloration experiments performed on Fe-doped $SrTiO_3$ reveal changes in the color of the anode/cathode regions over time. The changes in color are attributed to a change in Fe impurity oxidation state from Fe^{+3} ions (colorless) to Fe^{+4} ions (reddish brown). Over time, the anode region is oxidized as witnessed by the change to a reddish brown color. Thus, the electrocoloration effect clearly indicates $V_O^{\bullet\bullet}$ migration to be a cause of dc breakdown of the insulation resistance in bulk ceramics.

In bulk ceramic actuators, the leading causes of breakdown are microcracking, delamination at the electrode interface, gas discharge, and oxygen vacancy migration. By

controlling processing to limit the amount of space charge, $V_O^{\bullet\bullet}$, voids, pores, and inclusions, the mechanisms responsible for aging, electromechanical degradation, and device breakdown may be limited, allowing for increased piezoelectric device lifetimes.

2.6.2 Thin Films

Unlike bulk ceramics, the aging and degradation of the piezoelectric response in thin films have not been studied by many researchers. This section reviews the observations that have been reported in this area.

2.6.2.1 Aging

Thin film dielectric aging is apparently controlled by the same mechanisms as in bulk ceramics, i.e. pinning of domain walls is responsible for the observed decreases in the dielectric constant.[26, 39, 40]

Kholkin et al.[3] measured the aging of the longitudinal piezoelectric coefficient in PZT ceramics and thin films by double beam interferometry. Their results, seen in Figure 2.19, illustrate that in films, in contrast to the bulk, the aging of d_{33} differs greatly from ε_{33}. For bulk ceramics, ε_{33} and d_{33} are similar, with aging rates of less than 1% per decade. For films, ε_{33} again ages at less than 1% per decade; however, d_{33} in films ages more rapidly at nearly 3% per decade. With this large difference in the aging rates for permittivity and piezoelectric response, the researchers concluded that different mechanisms are responsible for each aging phenomenon. Aging of ε_{33} in both thin films and ceramics is believed to be due to pinning of domains; while, the decrease in d_{33} in thin films was attributed to a loss of polarization through what they called a "spontaneous" depoling. A decrease in the net polarization of the material lowers the

piezoelectric response as a result of the coupling between the piezoelectric response and polarization through the electrostrictive effect (see equation 2.11).

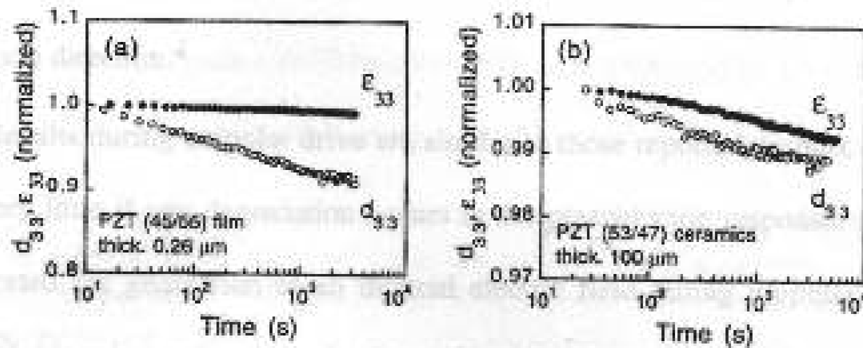

Figure 2.19: Aging of the longitudinal piezoelectric coefficient and the dielectric constant for a) a PZT thin film and b) a PZT ceramic.[3]

Similar results for the aging of the transverse piezoelectric response have been reported by Shepard et al.[9] By using the wafer flexure technique[5] to measure d_{31}, they confirmed the existence of rapid aging phenomena in the transverse piezoelectric coefficient with aging rates of 3 – 10% per decade observed in sol-gel PZT thin films. They also concluded that "spontaneous" depoling may be responsible for the rapid aging of the piezoelectric coefficient.

2.6.2.2 Electromechanical Degradation

Relatively little has been reported on the changes in the piezoelectric response of PZT thin films under bipolar and unipolar drive. Kholkin et al.[4] reported on the behavior of d_{33} under both of these operating conditions. They illustrated that during bipolar drive with field amplitudes greater than the coercive field, the piezoelectric response in PZT starts to decline after 10^3 cycles in response to a reduction in the polarization during cycling. This result agrees with the many reports in the literature of polarization fatigue

in which a decrease in remanent polarization commences near $10^3 - 10^5$ bipolar cycles. In addition to the decrease in d_{33}, Kholkin et al. witnessed a polarization offset during cycling. The origin of the fixed polarization was attributed to development of a preferred polarization direction.[4]

Results during unipolar drive are similar to those reported on bulk ceramics,[27] in which very little if any degradation occurs in the piezoelectric response. Kholkin et al. also reported the generation of an internal electric field during unipolar cycling. The internal bias is generated as a result of trapping of charge carriers which are injected from the metal electrodes.[4]

Currently, a specific knowledge of the reliability of the transverse piezoelectric response and the mechanisms responsible for its degradation in thin films is limited. Using knowledge of the mechanisms that are responsible for piezoelectric and dielectric degradation in bulk ceramics, this thesis determines the essential factors responsible for controlling reliability in PZT thin films. Additionally, improvements upon the initial reliability are demonstrated by altering the distribution of internal space charge and controlling the location of impurity defects.

Chapter 3: Experimental Procedure

3.1 Film Production

PZT thin films with a Zr/Ti ratio of 52/48 were deposited by a sol-gel spin coating process. Films were synthesized using a modification of the procedure described by Budd, Dey, & Payne.[41] Lead acetate trihydrate (Aldrich Chemical, Milwaukee, WI) was dissolved in 2-methoxyethanol at 110° C for 15 minutes in a rotary evaporator rotating at 120 rpm. The mixture was vacuum distilled at 110° C until either a paste or powder remained. The remaining material was then combined with a mixture of titanium-IV isopropoxide, zirconium-IV propoxide, and 2-methoxyethanol (Aldrich Chemical, Milwaukee, WI). The resulting solution was then refluxed at 110° C for 2.5 hours. Finally, 4 vol % formamide (Aldrich Chemical, Milwaukee, WI) was added to the resulting solution as a drying control agent with a resultant PZT concentration of 0.4 M.

The solutions were then spin coated onto either a 7.6 cm or 10.2 cm diameter platinized (100) silicon wafers (Nova Electronics, Richardson, TX). The wafer surface had a 1 μm thermal oxide, a sputtered 200 Å titanium buffer layer, and a 1500 Å sputtered platinum layer. The substrates were first blown clean with ultra high purity nitrogen and dried on a hotplate at 340° C for 1 minute. Using a P-6000 spin coater (Specialty Coating Systems, Indianapolis, IN), a vacuum was used to hold the wafer onto a chuck. A syringe with a 0.1 μm Whitman filter (Aldrich Chemical, Milwaukee, WI) was used to deposit solution onto the stationary substrate until complete coverage was obtained. The substrates were then spun at 3000 rpm for 30 seconds. The resulting sol-gel layer was pyrolyzed at 340° C for 1 minute. The deposition and pyrolysis process

was repeated 4 times before a crystallization step was performed. A Heatpulse 610 rapid thermal annealing furnace (A.G. Associates, San Jose, CA) was used to complete crystallization using a dwell at 700° C for 30 seconds. Deposition continued until a final film thickness ~1.0 μm was achieved.

3.2 Electrical Contacts

Top electrodes of platinum were deposited on the crystallized films by glow discharge sputtering through a 1.5 mm diameter shadow mask. A post-anneal at 385° - 400° C for 60 seconds was performed to remove sputtering-induced surface damage or contamination at the film-electrode interface. Two methods were utilized to make contact to the capacitors. One method involved using micro positioners (Signatone, Gilroy, CA) with fine tungsten tips to make a pressure contact with the platinum. Alternatively, a 2 cm long steel wire was attached perpendicular to the film surface near the top electrode with Circuit Works conductive epoxy (Chemtronics Inc, Kennesaw, GA). The epoxy contacted a small section of the Pt electrode. The steel wire was used as a connection post to solder an electrical lead from a panel of switches (so that many capacitors could be measured in tandem). The measured dielectric properties of the films did not depend on the contact method. Figure 3.1 illustrates the electrical circuit for connecting to the measuring instrumentation. By changing the inputs to the HI and LO lines, ferroelectric, dielectric, and piezoelectric measurements can be made on numerous samples in a short period of time.

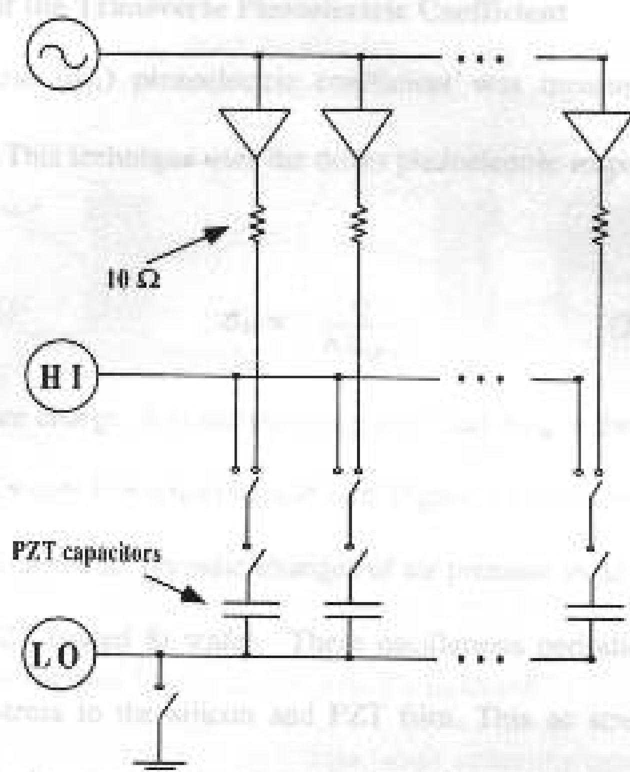

Figure 3.1: Schematic of the electrical connections used in making contact with the capacitors and performing dielectric and piezoelectric measurements. During cycling an ac voltage is applied to each sample using a buffer microchip to ensure a stable signal. By changing the connections to the HI and LO lines, ferroelectric, dielectric, and piezoelectric properties of individual capacitors could be measured.

3.3 High and Low Field Ferroelectric and Dielectric Characterization

Measurements of the remanent polarization, P_r, and the coercive field, E_c, were performed using a RT66A ferroelectric tester (Radiant Technologies, Albuquerque, NM). Typically, the maximum applied voltage ranged from 15 to 50 volts depending on film thickness. Low field measurements of the dielectric constant and dielectric loss were performed using a 4192A LF impedance analyzer (Hewlett-Packard, Palo Alto, CA). All low field experiments were performed at a frequency of 10 kHz with a peak-to-peak voltage of 30 mV.

3.4 Measurement of the Transverse Piezoelectric Coefficient

The transverse (d_{31}) piezoelectric coefficient was measured using the wafer flexure technique.[5] This technique uses the direct piezoelectric response to determine the film d_{31} via:

$$d_{31} = \frac{Q}{AX_{film}}, \qquad (3.1)$$

where Q is the surface charge, A is the electrode area, and X_{film} is the biaxial stress on the PZT thin film. The wafer flexure technique (see Figure 3.2) uses the oscillation of a 10 inch audio speaker to generate periodic changes of air pressure in an aluminum air cavity housed beneath a PZT coated Si wafer. These oscillations periodically flex the wafer, applying a biaxial stress to the silicon and PZT film. This ac stress creates a surface charge through the direct piezoelectric effect. The resulting rms current, i_{rms}, is monitored by a 7260 DSP Lock-In Amplifier (EG&G, Wokinham, UK). The charge, Q, is determined from the measurement of the rms current as

$$Q = \frac{i_{rms}}{2\pi f}, \qquad (3.2)$$

where f is the frequency of the pressure oscillations. To determine the stress on the film, a pressure transducer is used to monitor the pressure in the air cavity. The rms output voltage from the transducer, measured by the lock-in amplifier, is converted to a known pressure from the transducer calibration standards. This pressure is then translated into radial and tangential stresses in the wafer and film using traditional beam bending mechanics.[5]

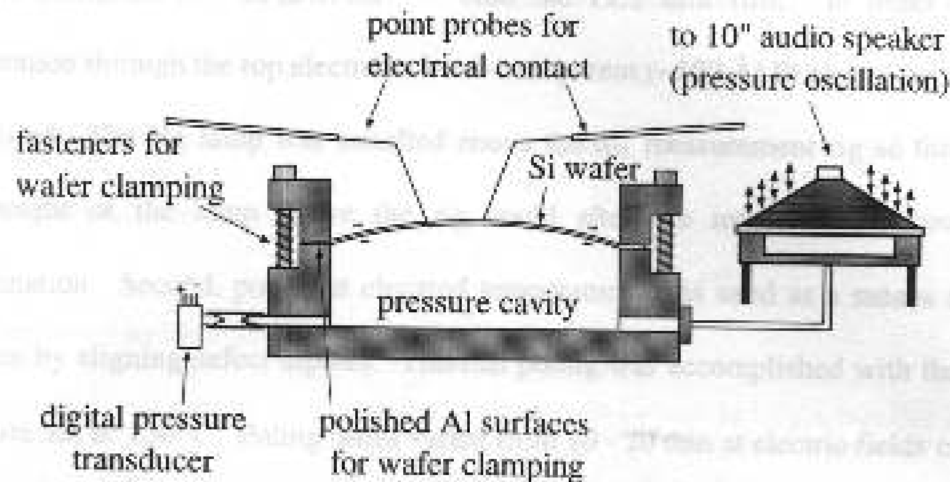

Figure 3.2: Schematic of the wafer flexure method. A PZT-coated Si wafer is clamped between Al rings (not to scale).[42]

3.5 Reliability of PZT Films Under ac Electric Field Drive

To determine the reliability of PZT films under operating conditions, a unipolar or bipolar ac electrical field was applied to the film and changes in the piezoelectric, ferroelectric, and dielectric properties were monitored over time. Typical values for the magnitude of the unipolar electric field ranged from 120 – 400 kV/cm, while that of the bipolar field ranged from 10 – 30 kV/cm. The frequency of the ac signal was 1 – 100 kHz. Experiments were initiated by poling the film with the resultant polarization directed towards the bottom electrode, aging for 5 min, measuring baseline values for d_{31}, ε_{33}, and tan δ, and then applying the electric field. Intermittently during cycling, the field was removed and the piezoelectric and dielectric properties were measured.

3.6 Imprint of PZT Films

Two procedures were followed to generate imprint in PZT thin films. In the first, samples were poled while illuminating with an ultraviolet (UV) radiation source. To accomplish UV-assisted poling, a 365 nm Hg source lamp (UVP Inc, Upland, CA) was

used to illuminate 25 – 50 mW/cm^2 onto the PZT thin film. In order to achieve penetration through the top electrode, semi-transparent (~150 Å) Pt electrodes were deposited. The Hg lamp was installed above the d_{31} measurement rig so that changing the height of the lamp above the rig could alter the intensity and power of the illumination. Second, poling at elevated temperatures was used as a means to generate imprint by aligning defect dipoles. Thermal poling was accomplished with the film on a hotplate set at 150° C. Poling times varied from 10 - 20 min at electric fields of 200 – 240 kV/cm.

3.7 HALT Measurements

Highly accelerated lifetime tests (HALT) were performed using Labview (National Instruments, Austin, TX) based software to monitor the current across a PZT thin film capacitor versus time. The setup enabled up to 30 electrodes to be monitored simultaneously. Samples consisted of a section of a 10.2 cm diameter silicon wafer. Multiple Pt electrodes were sputtered onto the PZT quarter wafers through a 1.5 mm diameter shadow mask. Contact with the HALT equipment was completed using epoxy and steel wire leads as mentioned earlier. However, for the HALT measurements, the conductive epoxy was Dupont 6838 silver epoxy (Dupont, Research Triangle Park, NC). HALT measurements were conducted at temperatures from 120 - 180° C with dc electric fields of 250 – 400 kV/cm.

3.8 Dielectric Breakdown

Using the HALT setup, multiple samples were monitored to determine the average breakdown field (E_B) for the PZT thin films at room temperature. Voltage

increments of 5 V were applied every 5 minutes to allow the film to equilibrate to the new electric field. As samples began to fail, the voltage increments were reduced to 1 or 2 V, again with 5 minute intervals between increases. This procedure was followed until all samples had failed.

3.9 Degradation Mechanism Characterization

Films exposed to extremely large electric fields can fail by a number of possible mechanisms including cracking, electrode delamination, and oxygen vacancy migration. To determine the extent to which these mechanisms promote failure, optical microscopy was used to locate surface anomalies such as surface cracks and charring. Both surface and cross-sectional analysis using scanning electron microscopy was performed to locate cracking and electrode delamination. Additionally, Auger electron spectroscopy (AES) depth profiling was used to measure the oxygen content near the top electrode film interface.

Chapter 4: Results and Discussion

4.1 Introduction

This chapter presents the results on the investigations into the reliability of the piezoelectric response in PZT thin films. The dielectric, ferroelectric, and piezoelectric properties were examined in response to aging and electric field stresses. Additionally, the affect of imprint on the reliability of these properties was studied with the goal of improving upon the initial reliability results. The long-term reliability of PZT sol-gel thin films under dc field was examined using the HALT technique. Lastly, the mechanism(s) responsible for dielectric and piezoelectric degradation were examined.

4.2 Ferroelectric, Dielectric, and Piezoelectric Properties

The PZT (52/48) thin films used in this investigation had primarily a <111> orientation with some degree of <110> and <100> orientation as well. These films possessed tilted polarization-electric field (PE) hysteresis loops. Figure 4.1 illustrates a typical PE loop for the sol-gel PZT thin films used in this investigation. Values of P_r ranged from 20 – 25 $\mu C/cm^2$ with an E_c ranging from 38 – 42 kV/cm. Additionally, these thin films possessed good dielectric properties with ε_{33} between 1000 – 1100 and a tan δ of 2 – 4%. Experiments throughout this thesis used a poling procedure with the top electrode being positively biased resulting in the polarization directed toward the bottom electrode. Using the wafer flexure technique, the transverse piezoelectric coefficient for the PZT thin films was evaluated with d_{31} values ranging from -25 to -40 pC/N. The dielectric breakdown strength (E_B) for the PZT thin films ranged from 250 – 800 kV/cm depending on film quality and thickness (0.7 – 1.3 μm).

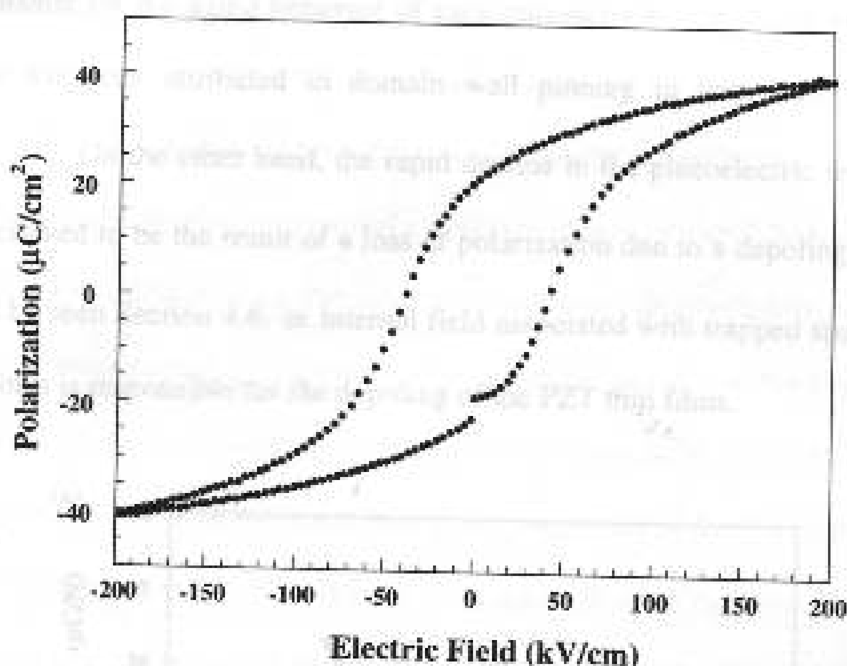

Figure 4.1: Polarization electric field hysteresis loop for a 1.0 μm thick PZT (52/48) thin film.

4.3 Aging

The aging of the dielectric and piezoelectric response has been well documented in bulk and thin film piezoceramics.[4, 9, 25, 26] The aging rates of the piezoelectric response in thin films are substantially larger than those of bulk ceramics with a rapid depoling possibly due to an internal electric field thought to be the mechanism responsible for the larger aging rates.

The PZT films used in this thesis research possess aging rates at room temperature and under dark conditions of 6 – 12% per decade for d_{31} and 1 – 2 % per decade for ε_{33}, which agrees well with values reported in the literature.[3, 9] Figure 4.2a illustrates how quickly the magnitude of d_{31} decreases during aging and Figure 4.2b shows the difference in the aging rates of ε_{33} and d_{31}. The presence of such a large difference in the aging rates of these two properties suggests that different mechanisms

are responsible for the aging behavior of each parameter.[3] The decay in the dielectric properties has been attributed to domain wall pinning in both bulk and thin film ceramics.[3, 26] On the other hand, the rapid decline in the piezoelectric response of thin films is believed to be the result of a loss of polarization due to a depoling mechanism.[3, 9] As will be seen Section 4.6, an internal field associated with trapped space charge and defect dipoles is responsible for the depoling of the PZT thin films.

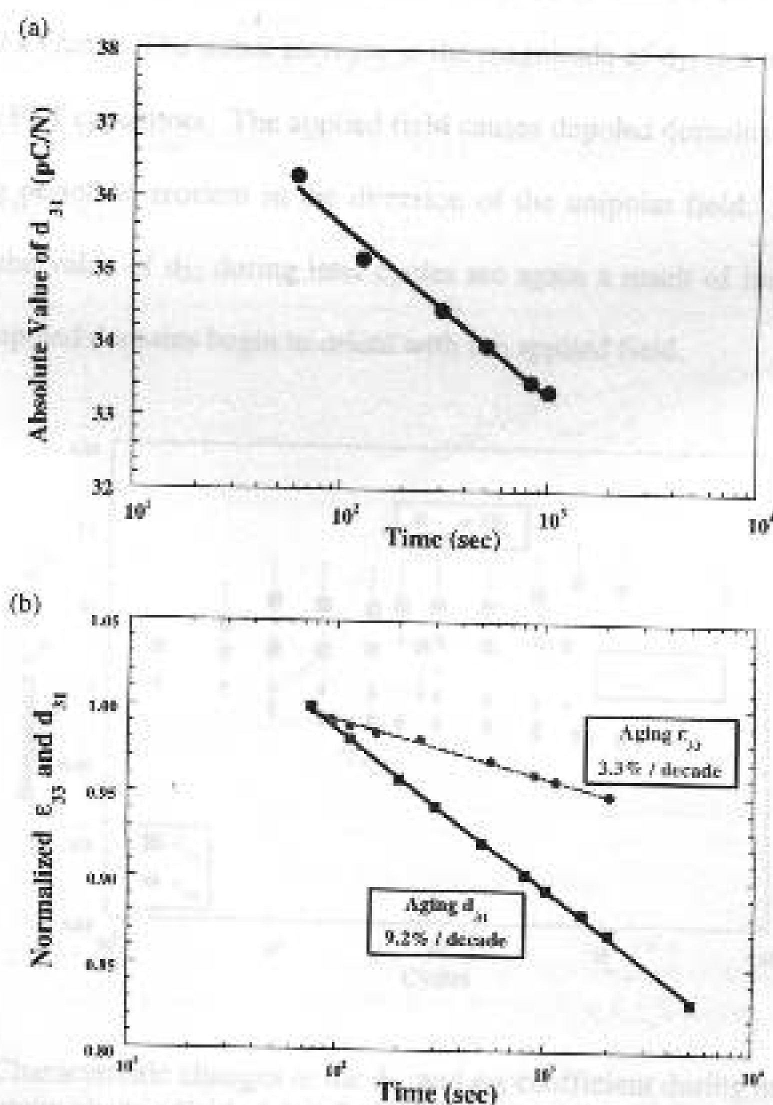

Figure 4.2: (a) Aging of the absolute value of d_{31} and (b) aging of the dielectric permittivity, ε_{33}, and the transverse piezoelectric coefficient, d_{31}.

4.4 Affect of a Unipolar ac Electric Field

In order to achieve large strains in a piezoelectric material, a large electric field must be applied. To assess the reliability of the transverse piezoelectric response under large electric fields, unipolar square and sinusoidal ac electric fields were applied to PZT piezoelectric capacitors. These devices have shown excellent reliability under varying amplitudes of unipolar fields. Figure 4.3 shows that devices can survive up to 10^9 cycles with no decrease in the piezoelectric response for electric field amplitudes from 3 - 5E_c (~120 - ~200 kV/cm). The initial increase in the magnitude of d_{31} is a result of improved poling of the PZT capacitors. The applied field causes depoled domains from the initial 5 minute aging period to reorient in the direction of the unipolar field. Additional slight increases in the value of d_{31} during later cycles are again a result of improved poling as previously unpoled domains begin to orient with the applied field.

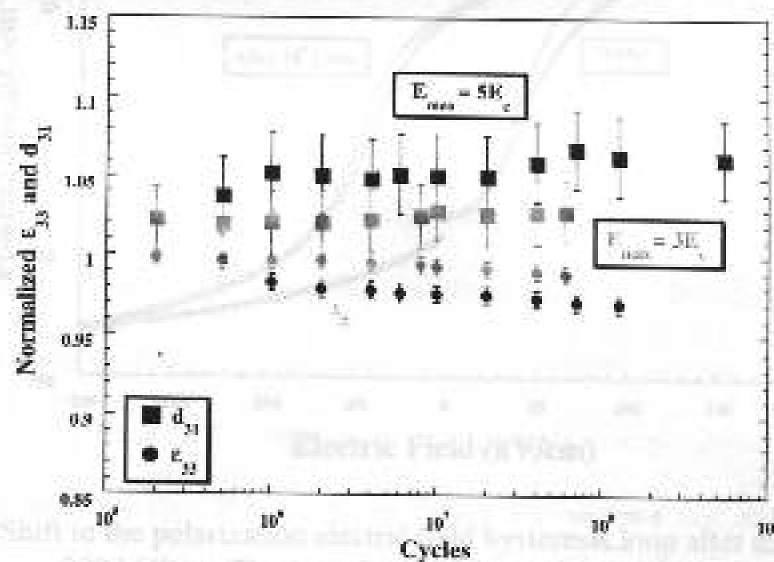

Figure 4.3: Characteristic changes in the d_{31} and ε_{33} coefficient during unipolar cycling with a maximum electric field of 3 and 5E_c (~120 - ~200 kV/cm). Error bars illustrate the range of values obtained in several experiments.

A second aspect of Figure 4.3 is the steady decline of ε_{33} during unipolar drive. This decline is probably related to a decrease in the extrinsic contribution to the dielectric constant by pinning or elimination of 180° domain walls. This may result from the internal field that is generated during cycling. This electric field is witnessed in Figure 4.4 by a shift in the PE hysteresis loop along the electric field axis. The shift has a magnitude of 4 – 6 kV/cm and increases the negative field required to switch the polarization from the positive remanent state. It is believed, given the low mobility of non-180° domain walls in PZT films under a micron in thickness,[15, 19] that the internal field is more important than changes in the extrinsic contribution to d_{31} in controlling the behavior during cycling.

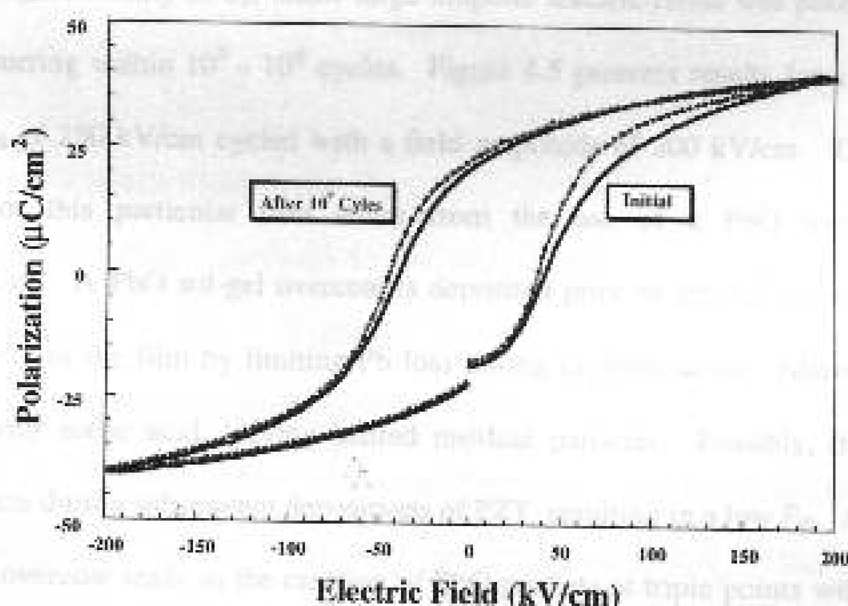

Figure 4.4: Shift in the polarization electric field hysteresis loop after unipolar drive at 200 kV/cm. The magnitude of the shift is 4.9 kV/cm.

The reliability of the thin film piezoelectric response obtained for unipolar drive agrees with the results of Wang et al.[27] for bulk PZT samples. They reported only slight

variations in d_{31} after 10^6 cycles. A stable piezoelectric response in thin films driven with a unipolar field was also reported by Kholkin et al.[4] Their study on the longitudinal piezoelectric response, d_{33}, in PZT thin films revealed a stable to increasing piezoelectric coefficient out to 10^8 unipolar cycles. They also observed the development of a piezoelectric coefficient-electric field hysteresis loop shift during unipolar cycling. By monitoring the change in E_c during cycling, they concluded the build up of an internal electric field was responsible for the shifts in the d_{33} electric field hysteresis loop and the rise in d_{33} during unipolar cycling.

Additional experiments using fields as high as $10E_c$ have been conducted with similar results. Again, stable d_{31} values occur to at least 10^9 cycles. However, for films with poor E_B, reliability of d_{31} under large unipolar electric fields was poor with sample failure occurring within $10^5 - 10^6$ cycles. Figure 4.5 presents results for a film with an average E_B of 250 kV/cm cycled with a field amplitude of 200 kV/cm. The extremely low E_B for this particular film arises from the use of a PbO overcoat during crystallization. A PbO sol-gel overcoat is deposited prior to crystallization to maintain stoichiometry in the film by limiting Pb loss during crystallization. Afterwards, it was removed with acetic acid, leaving behind residual particles. Possibly, these particles create defects during subsequent depositions of PZT, resulting in a low E_B. Alternatively, if the PbO overcoat leads to the creation of PbO pockets at triple points within the film, these would also lower E_B. The results in Figure 4.5 indicate that device reliability is reduced with a reduction in the breakdown field. The fast decrease in d_{31} is probably attributed to either delamination or microcracks that initiate during cycling (see Section 4.8.1).

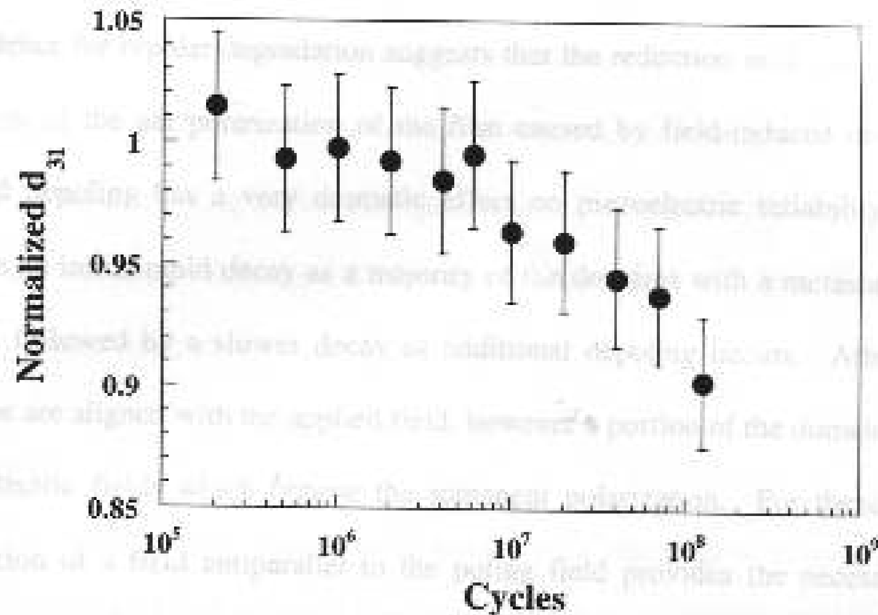

Figure 4.5: Representative results for PZT thin films with low breakdown fields (~250 kV/cm) cycled with a unipolar field of 200 kV/cm. Ranges given show sample-to-sample variations.

4.5 Bipolar ac Electric Field Drive

If film depoling contributes to the rapid aging behavior, then cycling with a bipolar electric field with a magnitude less than E_c should result in even faster degradation rates by field induced depoling. If the film starts initially poled at positive remanence, then any perturbation with a negative electric field will result in some degree of polarization switching as a result of the non-square nature of the PE hysteresis response. Thus, the larger the magnitude of a bipolar ac electric field, the greater the degree of polarization reversal. Figure 4.6 confirms the amplitude dependence of the bipolar degradation behavior. As the amplitude approaches E_c, there is a dramatic decrease in the d_{31} response during cycling. With amplitudes of $\frac{3}{4}E_c$, the d_{31} value drops

to 30% of it original value after 10^7 cycles. The existence of a large amplitude dependence for bipolar degradation suggests that the reduction in d_{31} is, in fact, due to a reduction in the net polarization of the film caused by field-induced depoling. Field-induced depoling has a very dramatic effect on piezoelectric reliability. The results indicate an initial rapid decay as a majority of the domains with a metastable orientation depole, followed by a slower decay as additional depoling occurs. After poling most domains are aligned with the applied field, however a portion of the domains may contain local electric fields which oppose the remanent polarization. For these domains, the application of a field antiparallel to the poling field provides the necessary energy to backswitch to a more stable domain configuration.

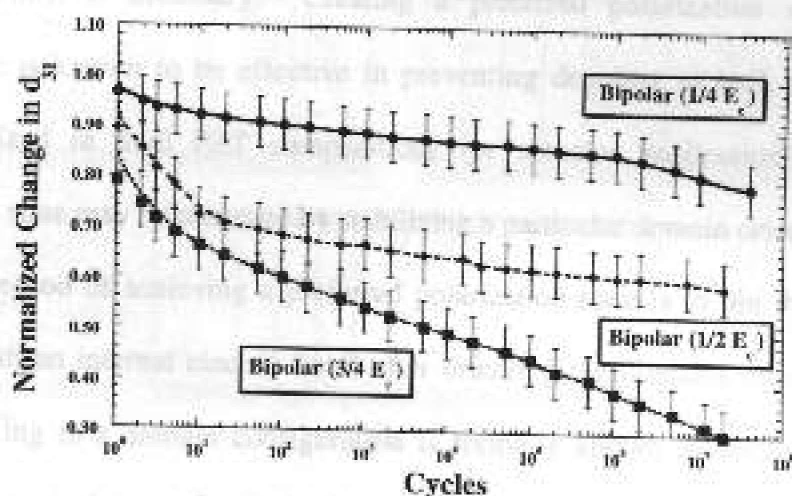

Figure 4.6: Amplitude dependence of bipolar degradation with each curve representing the typical behavior observed at a specified cycling field. The strong amplitude dependence indicates field induced depoling is the mechanism responsible for the decrease in d_{31} with cycling. The ranges given are indicative of sample-to-sample variability.

Monitoring the temperature of a sample during cycling was conducted with a 30 gauge thermocouple wire placed on the film within ~1 mm of the measured top electrode and held in place with a small section of scotch tape. It is assumed that the temperature is

uniform in the vicinity of the driven sample due primarily to the large thermal conductivity of the underlying silicon substrate. Investigations monitoring the temperature of the PZT capacitors resulted in a temperature change of ~2 – 5 °C during cycling. This small temperature change is insignificant and will not cause a substantial degree of depoling. Therefore, field-induced depoling is the most likely mechanisms causing the decline in d_{31} during cycling.

4.6 Imprint to Improve Reliability

To improve upon piezoelectric reliability, a mechanism to prevent depoling in PZT thin films is necessary. Creating a preferred polarization state within the ferroelectric is known to be effective in preventing depoling in bulk ceramics, and is widely utilized in hard PZT compositions for actuator applications. A preferred polarization state may be achieved by stabilizing a particular domain orientation.

A method of achieving a preferred polarization state is to pin the domain walls (perhaps with an internal electric field) after orienting the domains during poling. The idea of locking in a domain configuration is formally known as imprint and has been extensively studied as a factor limiting reliability in ferroelectric memories (where repetitive switching is required).[39, 40, 43] Imprint is observed as a voltage shift in the polarization hysteresis loop and has been proposed to be a result of domain pinning by space charge or defect dipoles.[43]

There are two main methods of achieving imprint. First, poling PZT films while illuminating them with ultraviolet radiation has been shown to shift the PE loop along the field axis.[43] Figure 4.7 is a schematic illustrating the mechanisms involved in UV generated imprint. Inherently, there is some degree of space charge present in PZT thin

films and as seen in Figure 4.7 it may reside in deep potential wells at domain boundaries. By using radiation with an energy greater than that of the band gap of PZT (~3.5 eV), electrons can be excited to the conduction band. As the electrons are removed from the traps along domain boundaries, the domains may align with an applied electric field as the free electrons reduce the electrostatic potential to domain reorientation.[43] The mobile charges migrate toward the electrodes, where, upon removal of the applied field, they become trapped and pin the domain walls in the aligned polarization configuration.

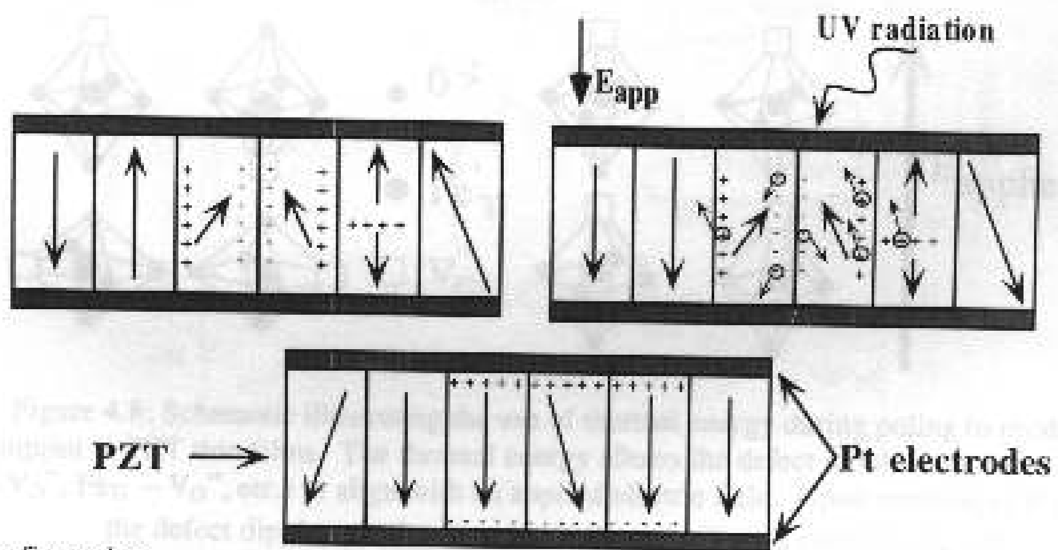

Figure 4.7: Schematic of the detrapping of electronic charges through the use of ultraviolet illumination during poling. Removal of the space charge at the domain boundaries allows locked domains to align with the applied electric field.[44]

The second method of achieving imprint utilizes the inherent point defects in sol-gel processed PZT and is seen in Figure 4.8. These defects include lead vacancies (V_{Pb}'') due to Pb volatilization, oxygen vacancies ($V_O^{\bullet\bullet}$) to compensate for the loss of Pb, and heavy metal impurities such as iron. The negative defects can associate with the positive oxygen vacancies and create defect dipoles. These dipoles, which are originally

randomly oriented in the film, create local internal electric fields that may be responsible for spontaneous depoling.[26] Additionally, these defect dipoles can pin domains and prevent switching.[45] $V_{Pb}'' - V_O^{\bullet\bullet}$ defect dipoles have a large energy barrier for reorientation and thus have a relatively low mobility at room temperature. By using elevated temperatures during poling, however, the thermal energy allows defect dipole complexes ($V_{Pb}'' - V_O^{\bullet\bullet}$, $Fe_{Ti}' - V_O^{\bullet\bullet}$, etc.) to align with an applied electric field.[46] The aligned defect dipoles increase the net polarization in the ferroelectric.

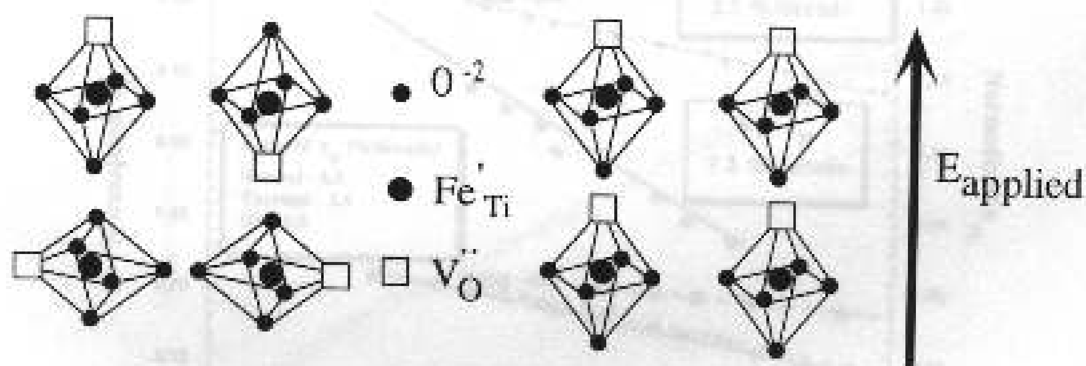

Figure 4.8: Schematic illustrating the use of thermal energy during poling to produce imprint in PZT thin films. The thermal energy allows the defect dipole complexes ($V_{Pb}'' - V_O^{\bullet\bullet}$, $Fe_{Ti}' - V_O^{\bullet\bullet}$, etc.) to align with an applied electric field. Upon removal of the field the defect dipoles pin the domains in the new aligned configuration.[44]

4.6.1 Affect of Imprint on Aging

Using the two imprint techniques discussed previously, dramatic improvements in the aging behavior occurred. Figure 4.9 presents the result of the various imprint procedures on the aging behavior. Thermal poling led to the greatest improvement, with initially larger d_{31} values and reduced aging rates of 2 – 3 %/decade. Thermal imprint increased the magnitude of d_{31} by 36% +/- 11% due to improved poling. Similar increases in the d_{33} piezoelectric response have been obtained on PZT thin films.[47] The thermal energy aligns a greater percentage of domains with the poling field. The

simultaneous alignment of defect dipoles with the applied electric field creates an internal electric field, shifting the PE loop on the field axis, and decreases the likelihood of progressive backswitching. Thus, in addition to larger piezoelectric coefficients, aging rates of d_{31} for thermally imprinted devices are significantly reduced.

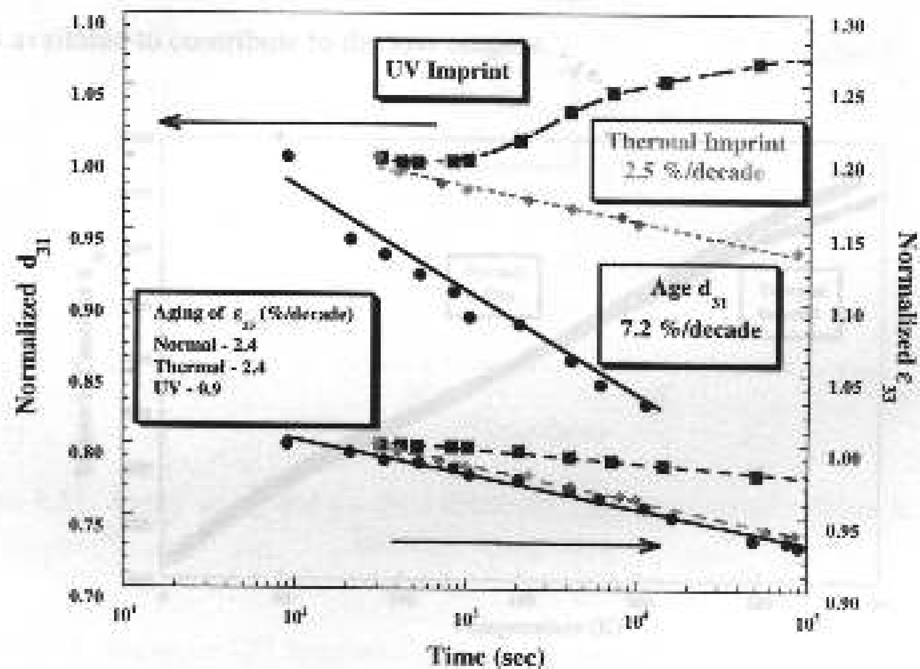

Figure 4.9: Imprint effects on aging. Thermal imprint reduces the aging rate from 7 – 10 %/decade to 2 – 3 %/decade. UV imprint results in non-linear aging because of an internal space charge field.

Additionally, thermal poling reduces the magnitude of the dielectric constant (~14 %) and loss tangent (~20 %). When samples were cooled to 4 Kelvin, the difference between normally poled and thermally poled samples disappeared (see Figure 4.10). This suggests that the decrease in ε_{33} at room temperature is due to decreased extrinsic contributions to the dielectric properties rather than the anisotropy associated with non-180° domain reversal. The decreased ε_{33} could be a result either of a reduction in the

density of domain walls or a decrease in domain wall mobility.[47] The reduction in tan δ could be due to a combination of this decrease in domain wall contributions, or to a decrease in the concentration of trapped space charge, or to more stable defect dipoles. As charge carriers are freed from deep traps because of thermal energy, they can annihilate with injected charges from the electrodes limiting the number of free charge carriers available to contribute to the loss tangent.

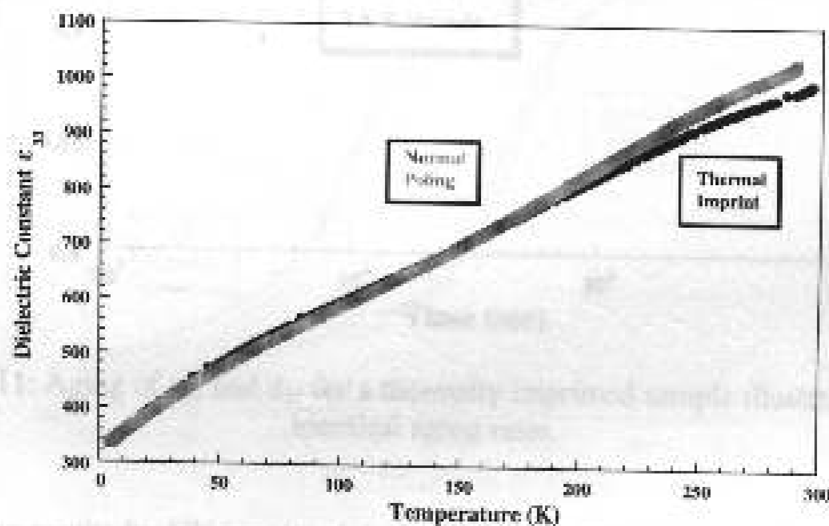

Figure 4.10: Affect of thermal imprint on the temperature dependence of ε_{33}. Differences in the room temperature dielectric properties for thermally imprinted and normally poled films are eliminated at 4 Kelvin.

As seen in Figure 4.11, after thermal imprint, d_{31} ages at nearly the same rate as ε_{33}. Thus, thermal imprint results in thin film piezoelectric aging rates approaching those experienced in bulk ceramics. Unlike bulk ceramics, two different mechanisms are responsible for the aging of the dielectric and piezoelectric responses. As stated previously, ε_{33} ages due to a decrease in 180° domain wall mobility. Because 180° walls do not contribute to the piezoelectric response, another mechanism is required to describe the aging of d_{31}. Similar to normally poled samples, the reduction in d_{31} over time is

believed to result from a depoling mechanism possibly due to an internal field associated with space charges. The thermal imprint acts to slow the rate of depoling.

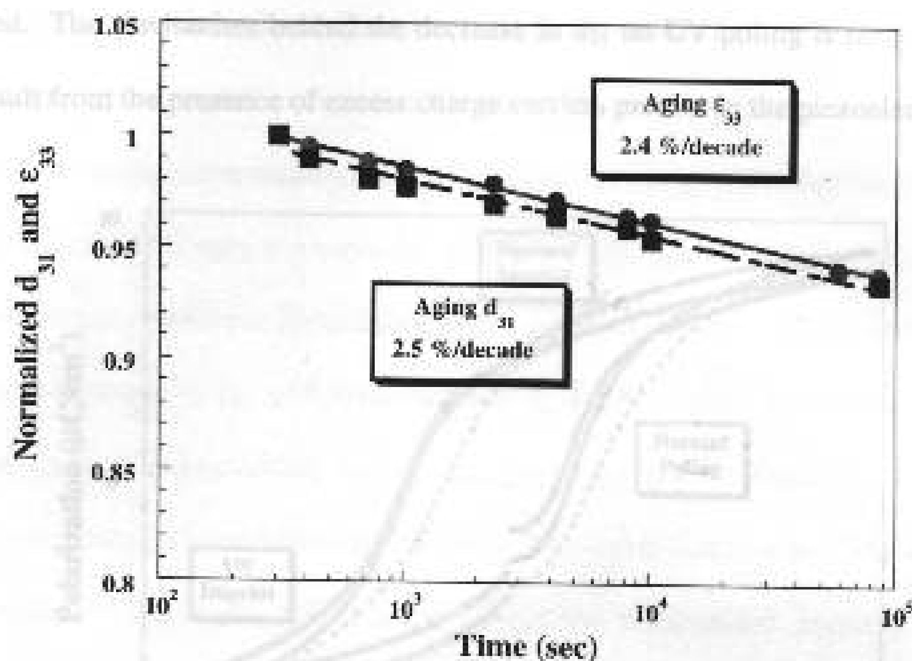

Figure 4.11: Aging of ε_{33} and d_{31} for a thermally imprinted sample illustrating nearly identical aging rates.

Aging results for UV imprinted devices are quite different from those of thermally imprinted devices. The dielectric constant is lowered by 11% +/- 3% relative to normally poled samples. The lower values of the dielectric constant can be explained by a reduction in 180° domain wall concentration or mobility as photo-induced charge carriers are trapped at domain boundaries after UV exposure. Relative to normal poling, UV imprint sometimes led to increases and sometimes to decreases in the piezoelectric response of up to 10%, depending at least in part on whether the capacitors were previously exposed to UV illumination during earlier experiments on other electrodes. The increases in the piezoelectric response agree with the results of Kholkin et al.[48] in which substantial increases in d_{33} occurred when films were subjected to UV illumination

during poling. Since the voltage shift generated is similar to that obtained by thermal imprint (as seen in Figure 4.12), a similar increase in the piezoelectric response might be expected. The mechanism behind the decrease in d_{31} on UV poling is not yet clear, but may result from the presence of excess charge carriers present in the piezoelectric.

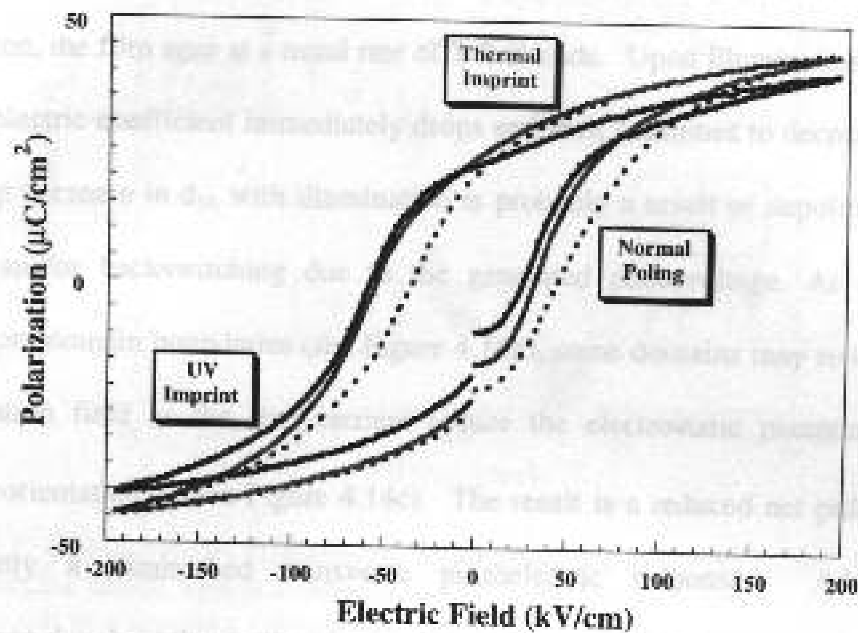

Figure 4.12 : Comparison of the voltage shifts in the PE loop of UV and thermally imprinted thin films.

After UV poling, the subsequent aging behavior of ε_{33} is normal, with reduced aging rates of -0.9 %/decade (see Figure 4.9). However, the aging behavior of d_{31} is non-linear (see Figure 4.9). Apparently, near 10^3 seconds after poling and exposure, there is a gradual increase in the value of the piezoelectric coefficient. This rise continues until $10^5 - 10^6$ seconds where the d-coefficient remains nearly constant or begins to decline.

To ascertain the mechanism(s) responsible for the aging behavior of the piezoelectric response in UV imprinted films, samples were normally poled, aged,

subsequently illuminated with UV radiation, and further aged. The goal was to determine whether a space charge field associated with photo-induced charges was responsible for the observed behavior in the transverse piezoelectric coefficient. The results from the experiments are presented in Figure 4.13 with schematics in Figure 4.14 presented to illustrate the mechanisms responsible for the behavior of d_{31} after illumination. Prior to illumination, the film ages at a usual rate of 7 %/decade. Upon illumination, the value of the piezoelectric coefficient immediately drops and then continues to decrease with time. This sharp decrease in d_{31} with illumination is probably a result of depoling of unstable domains and/or backswitching due to the generated photovoltage. As electrons are excited from domain boundaries (see Figure 4.14b), some domains may reorient with the depolarization field as the free carriers reduce the electrostatic potential barrier for domain reorientation[43] (see Figure 4.14c). The result is a reduced net polarization and subsequently a diminished transverse piezoelectric response. Additionally, a photovoltage develops due to the photovoltaic effect. This field is oriented anti-parallel with the direction of the polarization and can be large enough to result in some degree of domain back-switching.[49] The result is a decreased P_{net} and d_{31}.

Continued decreases in d_{31} during exposure may occur as charge carriers migrate due to the photovoltaic effect. Photo-generated charges migrate under the influence of the polarization potential.[49] The resulting build up of free carriers acts to shield the polarization potential and generates a photovoltage across the sample.[49] Therefore, during illumination an internal field develops opposing the direction of polarization (see Figure 4.14d). This field reduces the net charge available for measuring the transverse

piezoelectric response. Thus, d_{31} diminishes during UV exposure as the magnitude of the internal field increases.

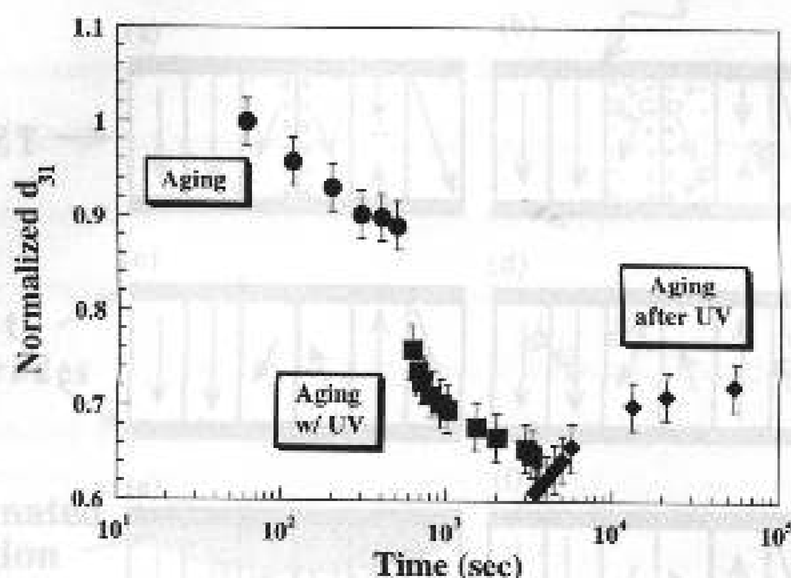

Figure 4.13: Changes in the piezoelectric response in response to UV illumination. Prior to exposure, the device ages at 7 %/decade. Upon illumination, there is a sharp decline in d_{31} *in response to a depoling mechanism. Subsequent decreases are the result of the build up of a space charge field. After illumination,* d_{31} *again drops but then begins to rise as the space charge field diminishes. Error bars are representative of the range of values observed among several similar experiments.*

Another possibility is that an internal field arises from the Dember effect.[50] A concentration gradient of charge carriers develops from non-uniform illumination through the sample depth due to a progressive drop in light intensity associated with absorption in the film and the top electrode.[48] Consequently, the charge carriers migrate to eliminate this gradient (see Figure 4.14e). The lower mobility of holes[43] reduces the diffusion distance compared to electrons, resulting in an internal electric field. This internal field will be directed toward the bottom electrode, only resulting in a net

decrease in piezoelectric charge for films with a polarization directed toward the top electrode.

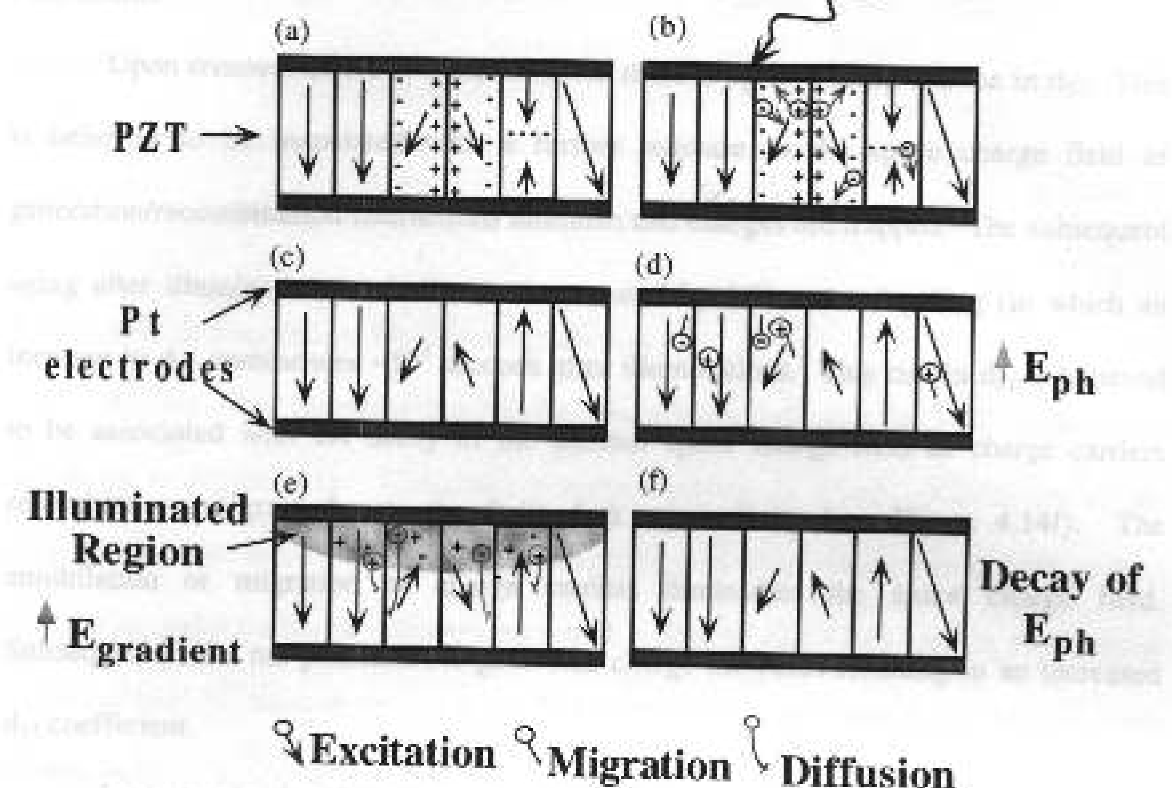

Figure 4.14: Schematics illustrating the mechanisms responsible for the aging behavior of UV exposed samples: (a) initial normally poled sample with the applied field (E_{app}) directed toward the bottom electrode, (b) photo-excitation of charge carriers by UV illumination, (c) metastable domains back-switch, aligning with depolarization field (E_{dep}), (d) migration of photo-induced charge carriers, resulting in a photoelectric field (E_{ph}), (e) development of an internal space charge field due to a charge carrier concentration gradient ($E_{gradient}$), (f) decay of the internal field due to migration and recombination of excess charge carriers.

UV illumination on poled samples with a positive and negative polarization state revealed similar behavior. The similarity in the aging behavior independent of poling direction eliminates a charge carrier concentration gradient as the controlling mechanism for the observed aging behavior. Thus, it is concluded that the continued decrease in d_{31}

during illumination results from an increasing internal field associated with the photovoltaic effect. The presence of this field reduces the net charge generated by the direct piezoelectric response, resulting in a lower value for the measured piezoelectric coefficients.

Upon removal of the UV illumination, there is again a sharp decline in d_{31}. This is believed to be associated with a further increase in the space charge field as generation/recombination interactions diminish and charges are trapped. The subsequent aging after illumination is similar to that created by UV assisted poling (in which an increase in d_{31} commences ~10^3 seconds after illumination). This rise in d_{31} is believed to be associated with the decay of the internal space charge field as charge carriers recombine or migrate due to the finite dark conductivity (see Figure 4.14f). The annihilation or migration of charge carriers diminishes the space charge field. Subsequently, the net piezoelectric generated charge increases resulting in an increased d_{31} coefficient.

Increases in d_{31} after post-poling illumination are limited to 3 – 5 % and are followed by a drop in d_{31} less than 10^5 seconds after exposure. In contrast, poling with illumination resulted in increases in d_{31} as a large as 10%, which are retained greater than 10^5 seconds after exposure. The shorter duration and lower magnitude of this increase for post-poling illumination suggests that the mechanism responsible for these increases is weaker in samples exposed to UV after normal poling. It is possible that a larger photovoltage is generated during UV assisted poling compared to that generated during the illumination of pre-poled samples. The larger photovoltage results in a larger internal field, thus creating an larger reduction in the net charge available to measure d_{31}.

From the results of these studies, it is concluded that both UV and thermal imprint can be utilized to improve aging. That is, the relatively modest electric fields that were built into the films via imprint were sufficient to stabilize the polarization and minimize depoling. Additionally, the development of an internal space charge during UV illumination limits the net charge generated from the direct piezoelectric response and results in diminished piezoelectric coefficients. The subsequent decay of this internal field after exposure increases the piezoelectric coefficient for a short duration.

4.6.2 Affect of Imprint on Bipolar Degradation

Imprint also improves the bipolar degradation behavior of PZT films, as is witnessed in Figure 4.15. Compared to normal poling, in which ~30% losses of the original d_{31} value were seen after 10^9 cycles, imprinted films retain at least 90% of their original d_{31} values after 10^9 bipolar cycles with a field of 20 kV/cm. Again, increases in d_{31} occur near 10^3 seconds for UV imprinted films due to a decrease in the internal space charge field.

The dielectric constant of thermally imprinted samples showed the same behavior as the piezoelectric coefficient as a function of bipolar cycling. Figure 4.16 illustrates the similarity in the two properties. There are several possible explanations for the observed increase in ε_{33} and d_{31} with cycling: an increase in temperature during cycling and an increase in the net polarization (P_{net}) by improved poling. That is, an increase in temperature could be caused by dielectric losses associated with the large ac fields. A small temperature rise would be expected to increase both ε_{33} and d_{31}. Alternatively, if imprint has shifted the polarization electric field hysteresis loop far enough along the electric field axis, then the application of a symmetric bipolar field may resemble

unipolar operation in a normally poled sample. Therefore, P_{net} may increase due to improved poling.

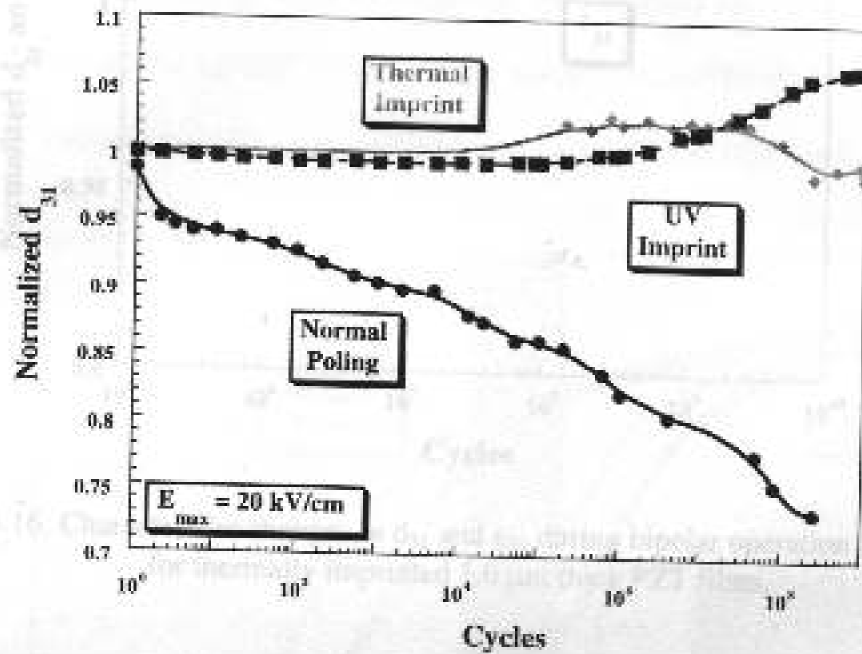

Figure 4.15: Affect of imprint on bipolar degradation illustrating the observed trends for each of the poling procedures.

To distinguish the relative importance of these factors, a variety of experiments were conducted. First, a polarization-electric field hysteresis loop was taken prior to and after bipolar cycling. From Figure 4.17, it is seen that a small voltage shift increasing the degree of imprint occurs during cycling. Examining the PE loops for imprinted and normally poled devices (see Figure 4.18), it is seen that a bipolar field of +/- 20 kV/cm traverses a less steep portion of the hysteresis loop for imprinted devices. Therefore, there is a reduction in the degree of polarization back switching during bipolar drive. It is possible that the continuous application of a field oriented parallel to the internal field acts to increase the remanent polarization, and hence d_{31}.

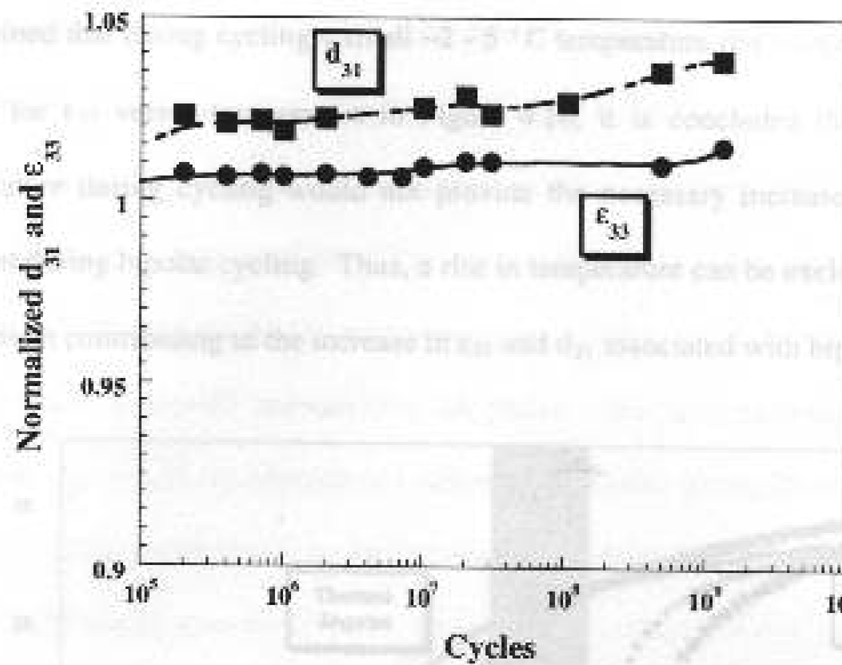

Figure 4.16: Characteristic changes in d_{31} and ε_{33} during bipolar operation (~20 kV/cm) for thermally imprinted 1.0 μm thick PZT films.

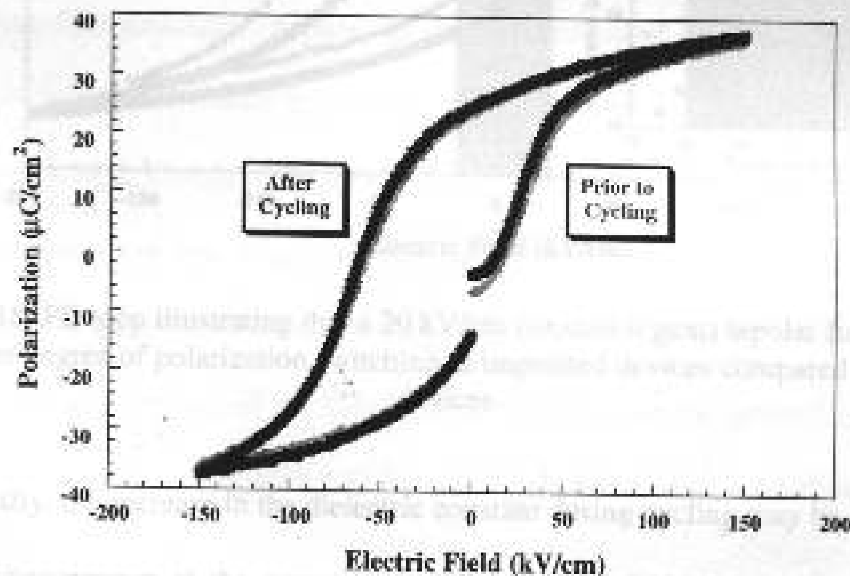

Figure 4.17: PE loops prior to and after bipolar operation.

Monitoring the temperature of a sample during cycling was conducted in the same manner as samples that were normally poled (see Section 4.5). Similarly, it was

determined that during cycling a small ~2 - 5 °C temperature rise occurs. Reviewing the results for ε_{33} versus temperature in Figure 4.10, it is concluded that this change in temperature during cycling would not provide the necessary increase in the dielectric constant during bipolar cycling. Thus, a rise in temperature can be excluded as a possible mechanism contributing to the increase in ε_{33} and d_{31} associated with bipolar drive.

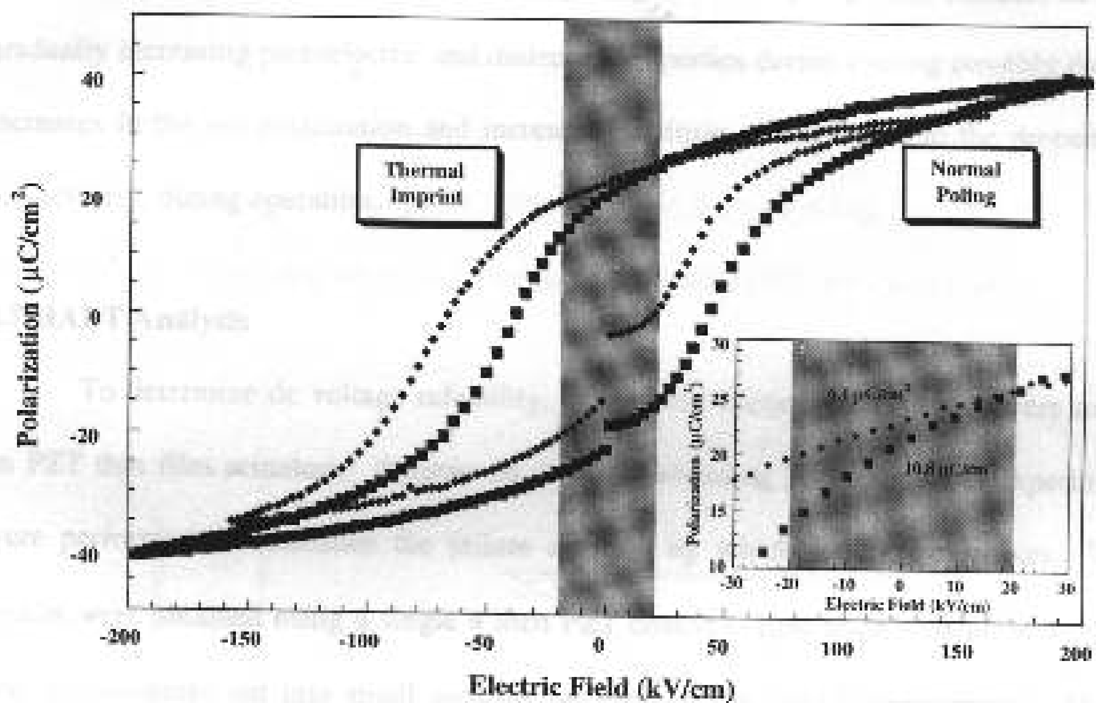

Figure 4.18: PE loop illustrating that a 20 kV/cm (shaded region) bipolar field provides a smaller degree of polarization switching in imprinted devices compared to normal devices.

Lastly, the increase in the dielectric constant during cycling may be attributed to a de-aging phenomenon as the concentration or mobility of 180° domain walls increase. Perturbations with an electric field oriented anti-parallel to the poling field may destabilize the positions of the walls, so that they can be readily perturbed by the

measuring field. This would increase the extrinsic contribution to the dielectric constant. The result is an increased ε_{33} during bipolar drive.

In summary, imprint can be used to improve device performance and lifetime under bipolar operating conditions. The space charge field generated during UV imprint plays a critical role in device performance with large increases in the piezoelectric coefficients occurring 10^3 seconds after UV poling. Thermally imprinted samples exhibit gradually increasing piezoelectric and dielectric properties during cycling possibly due to increases in the net polarization and increased extrinsic contributions to the properties, respectively, during operation.

4.7 HALT Analysis

To determine dc voltage reliability, accelerated lifetime experiments were made on PZT thin film actuators. A series of experiments using 30 samples per experiment were performed to determine the failure mode(s) by which breakdown occurs. The results were obtained using a single 4 inch PZT coated (~1μm thick) silicon wafer that was subsequently cut into small sections for each of the HALT experiments. Using electric fields of 250 – 400 kV/cm and temperatures ranging from 120 °C to 180° C, the room temperature lifetime of the piezoelectric samples can be determined in a HALT technique. The room temperature failure time is calculated using the following empirical relationship:

$$\frac{t_1}{t_2} = \left(\frac{V_2}{V_1}\right)^{-N} \exp\left[\frac{E_a}{k}\left(\frac{1}{T_1} - \frac{1}{T_2}\right)\right], \tag{4.1}$$

where subscripts 1 and 2 describe the test conditions, t is median time to failure (MTF), V is voltage, N is the voltage acceleration factor, E_a is the activation energy for failure, k is the Boltzmann constant, and T is temperature (K).[34]

The results from a typical experiment are presented in Figure 4.19. It is clear that there is wide scatter in the leakage current prior to breakdown. This scatter arises as the leakage currents are near or below the noise level of the instrumentation. Even with the scatter in the data, the general trend of a gradually increasing current prior to failure is present. Because of the scatter, failure was determined at the time the leakage current abruptly increased to ~10^{-3} amperes rather than the time at which the leakage current increased an order of magnitude with respect to the steady state leakage current.

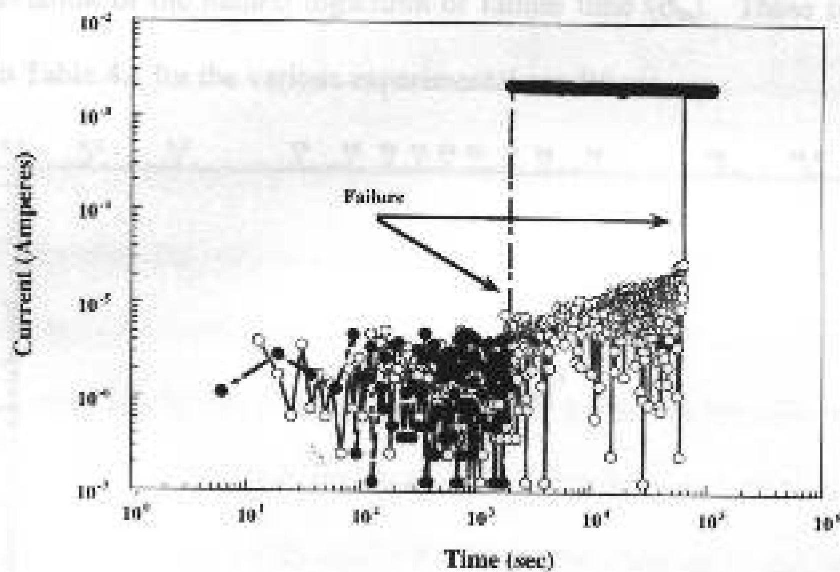

Figure 4.19: Plot of leakage current versus the time illustrating that failure occurs as an abrupt increase in the leakage current

The first step in the analysis is to determine if more than one failure mode is responsible for breakdown. This was done by reviewing the cumulative percent failure (cpf) versus log time plots in which deviation from linearity indicates the possible

presence of more than one failure mode. The method of acquiring these plots is given in Appendix A with the assumption that the data followed a logarithmic normal distribution. The calculated cpf plot for a temperature of 180° C and a field of 250 kV/cm is presented in Figure 4.20. As seen in Figure 4.20, an S-shaped curve results, indicating that a mixture of failure modes is responsible for breakdown in the specimens. The lower portion of the curve is associated with freak failures, typically a result of pores, voids, and delaminations due to processing defects.[51] Focusing on the upper portion of the curve, the median time to failure (MTF) and standard deviation can be calculated using the technique described in Appendix A. Assuming a log normal distribution, the MTF is the time for 50% failure (t_{50}) and the standard deviation is the shape parameter, the standard deviation of the natural logarithm of failure time (σ_{ln}). These two values are presented in Table 4.1 for the various experimental conditions.

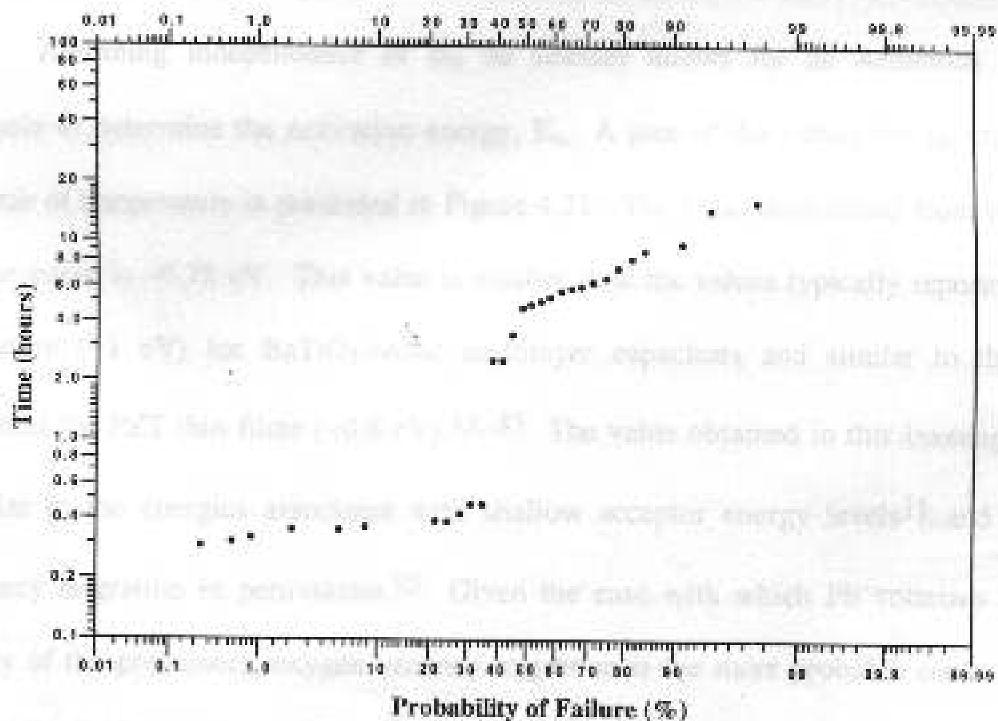

Figure 4.20: Cumulative percent failure plot for HALT test conducted with a field of 250 kV/cm and at a temperatures of 180° C.

As shown in Table 4.1, there is a small variation in the σ_{ln} values. If the mechanism responsible for failure is independent of the thermal and voltage stresses, then σ_{ln} should be constant. The reason for variation in these shape parameters may be due to the limited sample size used in this investigation and slight errors associated with using a graphical technique to determine the MTF and σ_{ln}.

Table 4.1: Results from HALT tests. Times are in hours.

Temperature (°C)	Voltage (V)	MTF (t_{50})	σ_{ln}
120	25	136	0.64
150	25	17	0.31
180	25	6.5	0.47
150	30	5.1	0.38
150	40	0.47	0.64

Assuming independence of σ_{ln} on stresses allows for an Arrhenius type of analysis to determine the activation energy, E_a. A plot of the values for t_{50} versus the inverse of temperature is presented in Figure 4.21. The E_a as determined from the slope of the curve is ~0.78 eV. This value is smaller than the values typically reported in the literature (~1 eV) for $BaTiO_3$-based multilayer capacitors and similar to the value reported for PZT thin films (~0.8 eV).[33, 35] The value obtained in this investigation is similar to the energies associated with shallow acceptor energy levels[11] and oxygen vacancy migration in perovskites.[52] Given the ease with which Pb volatizes and the purity of the precursors, oxygen vacancy migration is the more probable cause of wear out in the PZT capacitors. The value obtained for the activation energy in this thesis is statistically more significant than the previous reports on PZT thin films because of the

full HALT analysis that was conducted and the larger sample size used in the investigation.

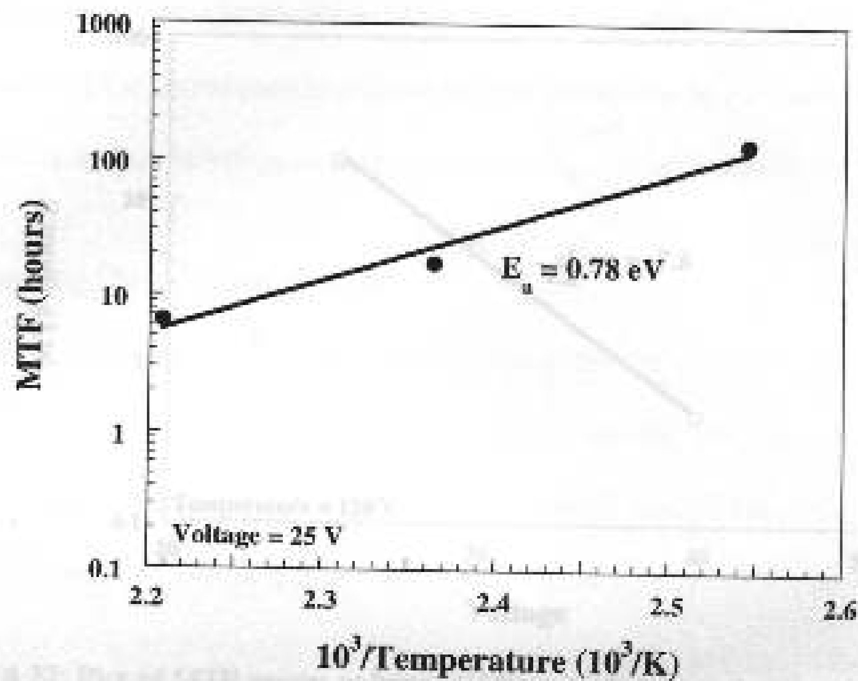

Figure 4.21: Plot of MTF versus 1/T determining the activation energy for failure. From the slope of the line, an E_a of 0.78 eV is calculated.

Similarly, a voltage acceleration factor can be determined. The MTF scales as the voltage raised to the power -N, where N is the voltage acceleration factor. Thus, plotting MTF versus the voltage on a log-log scale will yield N. Figure 4.22 illustrates the exponential dependence of t_{50} on voltage. From the curve, a voltage acceleration factor of 7.8 is determined which is larger than that reported for multilayer capacitors. Reports for multilayer capacitors present N as being between 2 – 3. [34, 35] For PZT thin films, Al-Shareef and Dimos report a value of 4 – 5. [33] The larger value for N obtained in this thesis might be due to extrinsic defects associated with processing which would lead to enhanced electric fields in the vicinity of the defect. Because the field is larger in the defect region, changes in the applied voltage can lead to earlier than expected failures.

Again, the work of Al-Shareef and Dimos was performed on a limited number of samples and may not provide a statistically significant value.

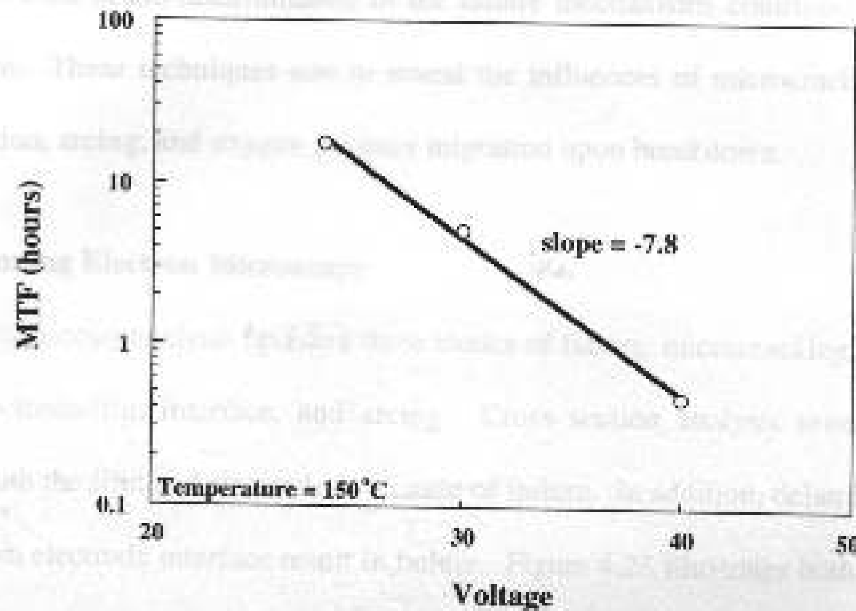

Figure 4.22: Plot of MTF versus voltage yielding a voltage acceleration factor of 7.8.

In summary, a statistical analysis of HALT data was performed as a means of developing an understanding of the failure modes responsible for breakdown. The results of the experiments reveal a substantial number of freak failures, suggesting that improved sample processing should increase reliability. This is not unreasonable given that the samples were not prepared in a clean room environment. Analysis at varying temperatures and voltages allowed for the determination of an activation energy, 0.78 eV, and a voltage acceleration factor, 7.8. These values suggest wear out of the PZT capacitors is due to oxygen vacancy migration. Additionally, a median time to failure can be determined for any operating condition from equation 4.1. For 1 μm thick devices performing at room temperature and at 10 V, the MTF is ~$1.4 \cdot 10^8$ hours.

4.8 Microscopy Analysis of Device Failure

Scanning electron microscopy (SEM) and Auger electron spectroscopy (AES) have been used in the determination of the failure mechanisms contributing to actuator breakdown. These techniques aim to reveal the influences of microcracking, electrode delamination, arcing, and oxygen vacancy migration upon breakdown.

4.8.1 Scanning Electron Microscopy

Microscopy analysis revealed three modes of failure: microcracking, delamination at the electrode/film interface, and arcing. Cross section analysis revealed cracking through both the film and electrode as a cause of failure. In addition, delaminations at the film/bottom electrode interface result in failure. Figure 4.23 illustrates both cracking and delamination in a PZT thin film. Clearly, both cracking and delamination result in sample failure. Because of the small thickness of the top electrode, it cannot be determined if delamination occurred at the top ceramic/electrode interface as it occurred at the bottom interface.

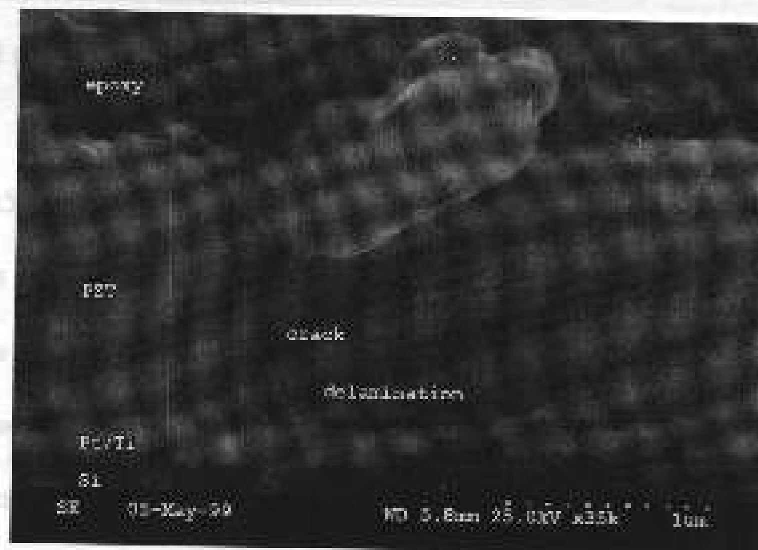

Figure 4.23: Scanning electron micrograph of cracking and delamination

In some instances, failure was clearly visible with the naked eye with the top electrode exhibiting a dark region where an arcing discharge has charred the electrode. In this case, the magnitude of the electric field is large enough to create a sputtering arc across a gap, which completely removes material from the contact area. Both PZT and the top Pt layers have been removed, leaving residual spheres of material (see Figure 4.24).

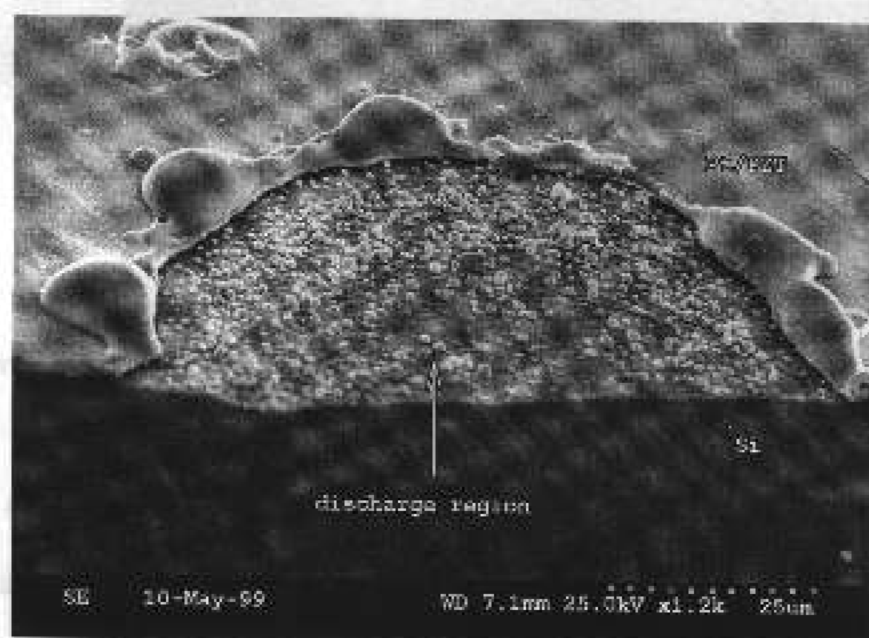

Figure 4.24: SEM micrograph of arcing revealing that the discharge region is riddled with tiny spheres of material.

Figure 4.25 revealed an interesting occurrence toward the edge of the discharge region. It appears as if the PZT has rolled over itself during the discharge. The brittle nature of ceramics should prohibit such behavior. One possible explanation is that local melting occurred which allowed PZT and Pt to flow and roll over the edges of the contact region. In this region, the arc does not have enough energy to dispel the material completely so it is pushed aside. The tight radius of curvature suggests that the curvature

may not be due only to tensile stresses that exist in the film due to thermal expansion mismatch.

Figure 4.25: Edge of arcing region showing the PZT film wrapped over itself, possibly due to peeling from the magnitude of stresses or a flash melting event.

Qualitative compositional changes across the discharge region were determined from a series of energy dispersive spectroscopy (EDS) scans. The results are presented in Figure 4.26. The analysis is based on the relative X/Zr peak height ratio, where X is any element. Four regions were analyzed: 1) the PZT thin film outside the damaged area, 2) the edge of the arcing region, 3) spheres located on the outskirts of the damaged area, and 4) spheres located in the center of discharge region. It is seen that the Pb/Zr ratio is large for the undamaged film. Moving toward the discharge area, the next scan was performed on the fold region where the Pb/Zr ratio is slightly reduced, indicating some degree of Pb loss. Inside the discharge region, the spheres showed a significant reduction in all peaks with the exception of Zr. Thus, the spheres within the arcing region are primarily a Zr based compound. Continuing to the position where contact was made with the point

probe it is seen that the Pb/Zr ratio is reduced even further. Therefore, in the vicinity of the arc there is enough energy to remove all components except Zr. Because Zr is the only component remaining after discharge, a review of the boiling points of zirconia and titania may develop an understanding of why Zr was not removed as the other elements. The boiling point of ZrO_2 is nearly double that of TiO_2 and substantially larger than that of PbO. If the vapor pressure scales as the inverse of the boiling point, PbO and TiO_2 should have higher vapor pressures compared to ZrO_2 at a given temperature. Therefore, it should be easier to remove PbO and TiO_2 from the PZT film, leaving behind residual ZrO_2.

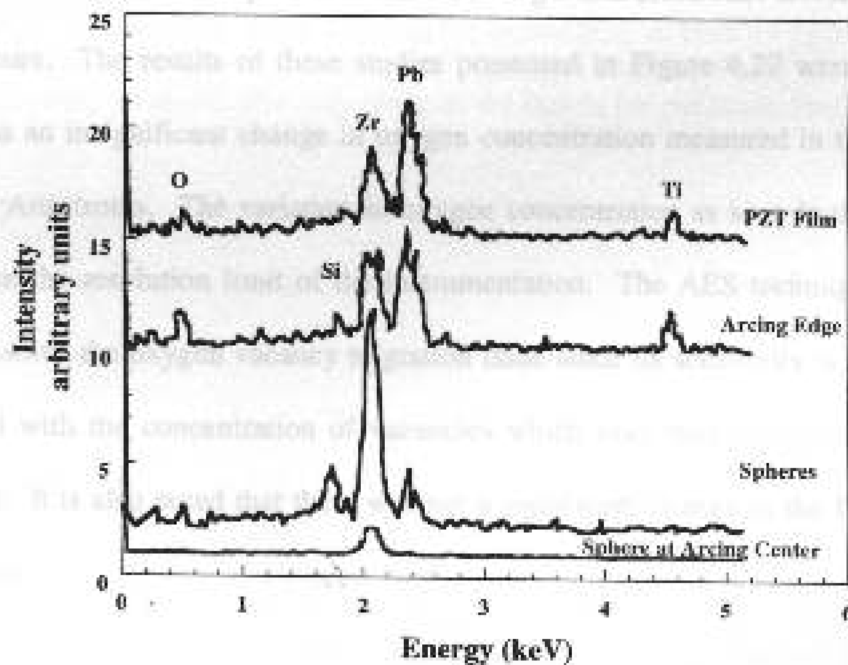

Figure 4.26: Results from energy dispersive spectroscopy on various regions in and around the arcing region.

From the microscopy analysis, it is concluded that the HALT samples breakdown by three main mechanisms. Microcracking and delamination conceivable are due to extrinsic processing induced defects. On the other hand, arcing may occur as result of

either extrinsic or intrinsic effects. While porosity and void space may provide the gap in which an arc can be struck, oxygen vacancy migration, as witnessed from the activation energy analysis in Section 4.7, may also provide a means for an arc to develop. As vacancies begin to migrate toward the cathode, the electric field concentration and current density may increase in the near electrode region. It is then conceivable as the current density rises during wear out that an arc can be generated resulting in breakdown.

4.8.2 Auger Electron Spectroscopy

In an attempt to ascertain whether oxygen vacancy migration may lead to failure in PZT thin films, AES was performed on both virgin and electrodes driven at 400 kV/cm for 48 hours. The results of these studies presented in Figure 4.27 were inconclusive. There was an insignificant change in oxygen concentration measured in the first several thousand Angstroms. The variation in oxygen concentration as seen in the two plots is lower than the resolution limit of the instrumentation. The AES technique may not be able to resolve the oxygen vacancy migration issue since its sensitivity is relatively poor compared with the concentration of vacancies which may lead to breakdown ($\sim 10^{18}$ – 10^{19} cm^{3}). It is also noted that there was not a significant change in the Pb content near the surface.

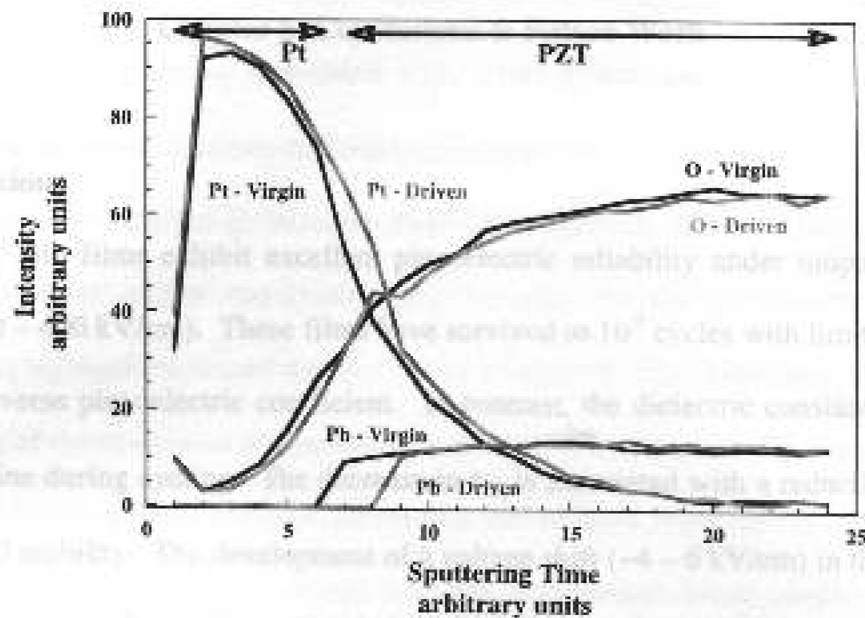

Figure 4.27: Results from Auger electron depth profiling on both a virgin sample and a sample driven at 400 kV/cm for 48 hours. Although all components of the PZT films were analyzed, the above plot only presents the results for platinum, lead, and oxygen.

Chapter 5: Conclusions & Future Work

5.1 Conclusions

PZT thin films exhibit excellent piezoelectric reliability under unipolar driving fields (~120 – 400 kV/cm). These films have survived to 10^9 cycles with limited changes in the transverse piezoelectric coefficient. In contrast, the dielectric constant exhibits a steady decline during cycling. The decrease in ε_{33} is associated with a reduction in 180° domain wall mobility. The development of a voltage shift (~4 – 6 kV/cm) in the PE loop during cycling provides evidence that indeed domains are pinned during the application of a unipolar field. As these walls become less mobile, the extrinsic contribution to the dielectric constant diminishes, resulting in lower values for ε_{33}.

However, the d_{31} coefficient exhibits rapid declines during both aging and bipolar cycling. The mechanism responsible for the large aging rates (6 – 12 %/decade) is field-induced depoling of domains due to the influence of internal electric fields generated by both space charges and defect dipole complexes. Similar to aging, a depoling mechanism is responsible for the rapid declines in the piezoelectric response during small amplitude bipolar drive. Under these operating conditions, the applied field induced depoling lowering the net polarization and resulting in a rapidly declining d_{31} coefficient.

Thermal and UV imprint improved the aging and bipolar degradation behavior of PZT thin films. The alignment of defect dipoles by thermal imprint increased the magnitude of d_{31} by 36% +/- 11% and reduced the piezoelectric aging rates to 2 – 3 %/decade. Improved poling was responsible for the increased piezoelectric response with a resulting stabilized domain configuration reducing d_{31} aging. In contrast to the

piezoelectric coefficient, the dielectric constant decreased after thermal imprint. This reduction in ε_{33} is possibly associated with either a decrease in 180° domain wall concentration or mobility during the imprint procedure.

UV imprint resulted in decreased dielectric properties, reduced aging rates for the dielectric constant, and a non-linear aging behavior for the piezoelectric response. Dielectric aging rates decreased nearly 50% to a value of −0.9 %/decade. On the other hand, aging of the transverse piezoelectric response exhibited a non-linear response with increases in the magnitude of d_{31} occurring near 10^3 seconds after imprint. This increase is the result of a decaying space charge field that is generated during imprint. The field develops from excess charge carriers introduced into the piezoelectric from photo-excitation. The resulting internal field limits the net charge generated by the direct piezoelectric effect, reducing the effective d_{31}. After a short time period the field begins to decay as the charge carriers redistribute, creating a gradual rise in the piezoelectric properties. The small dark conductivity of PZT allows the field to remain for nearly a day after illumination. Thus, it is concluded that internal electric fields associated with both trapped space charge and defect dipoles are responsible for the large d_{31} aging rates associated with PZT thin films.

Similar to the aging results, imprint improved bipolar degradation behavior. Again, UV imprint resulted in increases in the piezoelectric coefficient near 10^3 seconds after poling with near zero degradation occurring after the space charge field had diminished. Thermal imprint also provided improvements in bipolar behavior with increases in both ε_{33} and d_{31} witnessed during bipolar cycling. The increase in the piezoelectric response resulted from an increase in the net polarization through improved

poling during cycling; while, the increase in the dielectric constant resulted from either an increase in 180° domain wall concentration or mobility.

HALT measurements were performed illustrating the feasibility of performing statistical approach to predict the lifetime of PZT thin films. The results from experiments revealed that dc operating reliability has two regimes. In the initial stages there is a finite percentage of freak failures due primarily to mechanisms associated with processing defects. Second, there exists a linear region in which failure is associated with a rapid failure associated. Fitting the lifetime data with a lognormal distribution allowed for a graphical determination of the two independent variables, the median lifetime (t_{50}) and standard deviation (σ_{ln}). Calculations of both the activation energy for failure and voltage acceleration factor were completed with a value of 0.78 eV for E_a and a value of 7.8 for the voltage acceleration factor.

5.2 Recommendations for Future Work

5.2.1 Develop Database for HALT Analysis on PZT Thin Films

In order to properly assess device lifetimes using an accelerated lifetime test, a larger database is required consisting of a large sample size for each variation in the stress conditions. Continuing the results of the HALT experiments presented in this thesis would allow a more accurate determination of both the activation energy for failure and voltage acceleration factor. This, in turn, should result in improved lifetime prediction under any operating conditions.

Additionally, a better control of the population of freak failures in the early stages of operation is required. Through improvements in cleanliness during sol-gel deposition

of PZT and subsequent sputtering of Pt, the film quality should increase as extrinsic processing defects such as voids, pores, and delamination regions are eliminated. Improvements in the electrical contact are also required to provide increased accuracy and precision in the HALT analysis. Possibilities include using pressure contacts such as probe tips or a liquid metal electrode to eliminate any additional stresses associated with using epoxy as the contact.

5.2.2 Ellipsometry as a Means of Measuring Oxygen Concentrations

To determine the role of oxygen vacancy migration in piezoelectric and dielectric reliability, spectroscopic ellipsometry could be used to determine if a variation in oxygen concentration throughout the film thickness exists after operation. Spectroscopic ellipsometry is a light reflection technique capable of depth profiling with resolutions typically on the order of angstroms. The changes in the phase and amplitude of the polarization components of the reflected light are characteristic of the depth profile of the dielectric function of the film.[53] Oxygen vacancies can be detected indirectly by monitoring color changes in the transition metal ions adjacent to the vacancies. In this manner, it may be feasible to detect changes in oxygen vacancy distribution prior and after operation. The kinetics of the gradual build up of oxygen vacancies near the cathode should allow for a quantitative analysis of the role oxygen vacancy migration plays in piezoelectric reliability.

5.2.3 Bombardment Induced Imprint

The reliability of the piezoelectric response for thin films grown by physical vapor deposition (PVD) methods (RF magnetron sputtering, pulsed laser deposition, ion-

beam sputtering) should be investigated with an attempt to generate imprint by using ion bombardment during deposition. Recent work by Maria[42] has shown that precise control of deposition conditions during the growth of $Pb(Mg_{1/3}Nb_{2/3})O_3$-$PbTiO_3$ thin films using pulsed laser deposition allowed the degree of imprint to be controlled.

Applying this process to other PVD techniques, the reliability of the transverse piezoelectric coefficient should be investigated with emphasis on aging, bipolar, and unipolar drive. Comparing the results from these studies with those achieved in this thesis should allow for comparison of the controlling mechanisms in piezoelectric thin film reliability. Bombardment induced imprint uses the high energy of the incoming ions to impart a preferred polarization state in the ferroelectric. The preferred polarization state generated during bombardment arises from stress relief and should not alter the space charge or defect dipole arrangements. Thus, by comparing the three imprint techniques, a clear understanding can be developed describing the roles of space charge, defect dipoles, and stress on the aging and electric field cycling degradation behavior.

5.2.3 Verification of a Photovoltaic Induced Internal Electric Field

Experiments designed to measure the thermally stimulated current on a PZT actuator can be used as a means of verifying that trapped space charge contributes to the non-linear aging behavior of UV imprinted films. To avoid the influence from changes in the polarization state of the film, the temperature should remain relatively low, far from the Curie Temperature of ~380° C. The current across the actuator could be monitored as the temperature is increased to ~150° C and subsequently decreased to room temperature. The current flow could be monitored on both heating and cooling, if possible. As the temperature increases, trapped charge should be liberated, causing an

increase in the current. The current may also increase due to thermal depoling. To measure the degree of thermal depoling, the transverse piezoelectric coefficient could be monitored prior to and after the temperature cycle. This procedure would then be repeated several times. The subsequent current versus temperature plots should show changes in the current upon thermal cycling. Taking into account the changes due to thermal depoling, increases in the current can be attributed to the liberation of trapped charge, thereby verifying the existence of trapped space charge and its contributing role in the non-linear aging behavior of UV imprinted samples.

5.2.4 Modeling Aging Behavior through a Modified Activation Barrier

As is shown in Section 4.6.1, imprint improves the aging behavior of PZT thin films. The generation of an internal field biases the PE hysteresis loop such that one polarization state becomes preferred. It may be possible to model the piezoelectric aging behavior by relating the internal field to a change in the activation barrier height for polarization reversal.

From ferroelectric phenomenology, it is known that the gradual build up of an internal electric field results in skewing of the free energy versus polarization curve such that one polarization state becomes preferred. This increases the activation barrier for switching among the possible polarization states by $\frac{E_{int}}{k_B T}$, where k_B is Boltzman's constant and T is temperature. With this understanding, it may be possible to quantify the aging rate of d_{31} (which is associated with depoling) through a modified activation barrier. As the magnitude of the internal field increases, the activation energy for polarization reversal increases, possibly reducing aging rates.

By biasing the PE loop varying degrees, the aging rate can be evaluated against the magnitude of the internal electric field. Additionally, the aging rate can be evaluated as a function of temperature for a device with a specific internal electric field. Comparing these two experimental results should reveal a quantitative relationship between the aging rate of PZT thin films and the activation energy for polarization switching.

5.2.5 Magnitude of Internal Electric Field as a Function of Unipolar Cycles

Preliminary results reveal that the magnitude of the voltage shift in the PE hysteresis loop varies linearly with the logarithm of the number of unipolar cycles. Additional experiments are necessary to provide statistical significance to this observation as well as to determine if the internal field saturates at later cycles. In addition, it would be interesting to note if the build-up of an internal electric field during unipolar cycling is frequency or temperature dependent.

Appendix

Device reliability is defined as the probability of survival during a distinct set of operating conditions.[51] The reliability function, R(t), describes the device survival rate at any time, t. This function can be determined from a set of failure times by using the cumulative distribution function of failure, F(t), with

$$R(t) = 1 - F(t). \qquad (A.1)$$

Failure rates are generally not linear with time so fitting the data is required to acquire an understanding of F(t).[51] The two most prominent distributions used to fit reliability data are the lognormal distribution, $f_{ln}(t)$, and Weibull distribution, $f_w(t)$, density functions. This description will focus on the lognormal distribution function, which is given by

$$f_{ln}(t) = \frac{1}{\sqrt{2\pi\sigma_{ln}^2}\, t} \exp\left[-\frac{1}{2}\left(\frac{\ln t - \ln t_{50}}{\sigma_{ln}}\right)^2\right], \qquad (A.2)$$

where t_{50} is the time at which 50% of the devices fail and σ_{ln} is the standard deviation of ln t. These two independent parameters describe the lognormal distribution and provide a direct link for the determination of the reliability function. The ln t_{50} is also referred to as the median lifetime (MTF). Additionally, σ_{ln} should be independent of all stresses for accelerated life testing to be applied.[51]

One method of determining the value for the two independent variables is through a graphical representation. First, the data set of lifetimes must be rank ordered from 1 to n (the sample size). Following this, the cumulative failure distribution function (CDF), F(t) is determined as follows:

$$F_i(t) = \frac{i - 0.3}{n + 0.4}, \qquad (A.3)$$

where i is the rank order and n is the sample size. From the CDF, the cumulative percent failure (cpf) is calculated by multiplying F(t) by 100. Next, using lognormal graph paper, the logarithm of the failure time, t, is plotted against the cumulative percent failure. For a lognormal distribution,

$$\ln t = \ln t_{50} + \sigma_{ln}(cpf). \qquad (A.4)$$

Therefore, the MTF is determined directly from the graph as the time for 50% failure. Graphically, the standard deviation is calculated from the slope of the line as follows:

$$\sigma_{ln} = \frac{1}{2}\ln\left(\frac{t_{84}}{t_{16}}\right), \qquad (A.5)$$

where t_{84} and t_{16} are the time to failure for 16 % and 84 % of the samples, respectively. The values of 16 and 84 are chosen because that is one standard deviation away from t_{50}.

S-shaped curves (see Figure A.1) require a slightly different approach. In this case, the failure is due to a mixture of two failure modes[54] so that the probability of failure is given as the sum of the probability of failure for modes A and B,

$$F_{obs}(t) = p * F(t)^A + (1 - p) * F(t)^B, \qquad (A.6)$$

where $F_{obs}(t)$ is the observed failure probability, p is the probability of failure, and $F(t)^A$ and $F(t)^B$ are the actual failure probabilities for modes A and B, respectively. Typically, type A failures are associated with freak failures due to processing defects. The inflection point where the slope abruptly changes between the lower and upper portions of the curve is taken as the point where B type failures begin to dominate at longer times. The value of p is taken as the inflection because at this point it is assumed that all type A failures have occurred so $F(t)^A$ equals unity.

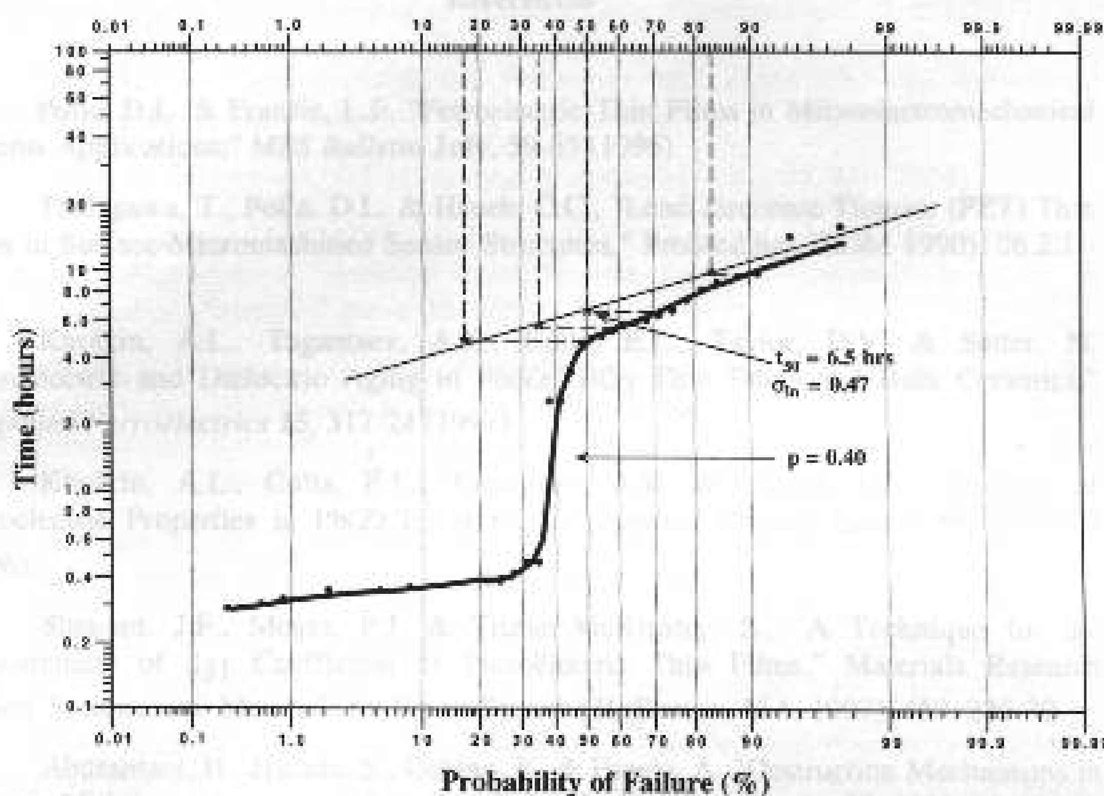

Figure A.1: Plot illustrating an S-shaped cdf curve and the graphical technique used to determine t_{50} and σ_{ln}.

Concentrating on the upper portion of the curve, the MTF and σ_{ln} must be determined from this curve. From a point on the linear portion of this curve, both the observed failure and actual failure for B type failures are noted. The actual failure, $F(t)^B$, is determined by plugging values into Equation A.6 and solving for $F(t)^B$, assuming that $F(t)^A$ is unity. The value obtained is then placed onto the graph at the appropriate location. This procedure is continued for other points in order to obtain a straight line for values of $F(t)^B$. Next, in a similar procedure as stated earlier, the values of $\ln t_{50}$ and σ_{ln} are calculated from the resultant line.

References

1 Polla, D.L. & Francis, L.F. "Ferroelectric Thin Films in Microelectromechanical Systems Applications," *MRS Bulletin* **July**, 59-65 (1996).

2 Tamagawa, T., Polla, D.L. & Hsueh, C.C., "Lead Zirconate Titanate (PZT) Thin Films in Surface-Micromachined Sensor Structures," Proceedings IEDM 1990), 26.2.1 - .2.4.

3 Kholkin, A.L., Tagantsev, A.K., Colla, E.L., Taylor, D.V. & Setter, N. "Piezoelectric and Dielectric Aging in $Pb(Zr,Ti)O_3$ Thin Films and Bulk Ceramics," *Integrated Ferroelectrics* **15**, 317-24 (1997).

4 Kholkin, A.L., Colla, E.L., Tagantsev, A.K. & Taylor, D.V. "Fatigue of Piezoelectric Properties in $Pb(Zr,Ti)O_3$ Films," *Applied Physics Letters* **68**, 2577-79 (1996).

5 Shepard, J.F., Moses, P.J. & Trolier-McKinstry, S., "A Technique for the Measurement of d_{31} Coefficient of Piezoelectric Thin Films," Materials Research Society Symposium: Materials for Smart Systems II (Boston, MA, 1997), 459, 225-30.

6 Aburantani, H., Harada, S., Uchino, K. & Furuta, A. "Destruction Mechanisms in Ceramic Multilayer Actuators," *Japanese Journal of Applied Physics* **33**, 3091-94 (1994).

7 Winzer, S.R., Shankar, N. & Ritter, A.P. "Designing Cofired Multilayer Electrostrictive Actuators for Reliability," *Journal of the American Ceramic Society* **72**, 2246-57 (1989).

8 Uchino, K., "Reliability of Ceramic Actuators," Proceedings of the Tenth IEEE International Symposium on Applications of Ferroelectrics (East Brunswick, NJ, 1996), 2, 763-6.

9 Shepard, J.F.,"The Investigation of Biaxial Stress Effects and the Transverse Piezoelectric (d_{31}) Characterization of Lead Zirconate Titanate Thin Films," Ph. D. Thesis, *The Pennsylvania State University*, 1998.

10 Jaffe, B., Cook, W.R. & Jaffe, H. *Piezoelectric Ceramics*,(R. A. N., Ohio, 1971).

11 Moulson, A.J. & Herbert, J.M. *Electroceramics*,(Chapman & Hill, New York, 1990).

12 Devonshire, A.F. "Theory of Ferroelectrics," *Advances in Physics* **3**, 85-130 (1954).

13 Cross, L.E. "Ferroelectric Ceramics: Tailoring Properties for Specific Applications," in *Ferroelectric Ceramics* (eds. Setter, N. & Colla, E.L.) 1-85 (Birkhauser Verlag, Boston, 1993).

14 Kanno, I., Fujii, S., Kamada, T. & Takayama, R. "Piezoelectric Properties of c-Axis Oriented $Pb(Zr,Ti)O_3$ Thin Films," *Applied Physics Letters* **70**, 1378-80 (1997).

15 Kholkin, A. "Electromechanical Properties and Domain-Related Effects in Ferroelectric Thin Films," ***Ferroelectrics to be published***.

16 Lefki, K. & Dormans, G.J.M. *Journal of Applied Physics* **76**, 454 (1994).

17 Zhang, X.L., Chen, Z.X., Cross, L.E. & Schulze, W.A. "Dielectric and Piezoelectric Properties of Modified Lead Titanate Zirconate Ceramics from 4.2 to 300K," *Journal of Materials Science* **18**, 968-72 (1983).

18 Zhang, Q.M., Wang, H., Kim, N. & Cross, L.E. "Direct Evaluation of Domain-Wall and Intrinsic Contributions to the Dielectric and Piezoelectric Response and Their Temperature Dependence on Lead Zirconate-Titanate Ceramics," *Journal of Applied Physics* **75**, 454-59 (1994).

19 Damjanovic, D. "Stress and Frequency Dependence of the Direct Piezoelectric Effect in Ferroelectric Ceramics," *Journal of Applied Physics* **82**, 1788-97 (1997).

20 In, T.-G. & Baik, S. "Leakage Current of Al- or Nb-doped $Ba_{0.5}Sr_{0.5}TiO_3$ Thin Films by RF Magnetron Sputtering," *Journal of Materials Research* **13**, 990-4 (1998).

21 Peng, C.-J. & Krupanidhi, S.B. "Structures and Electrical Properties of Barium Strontium Titanate Thin Films Grown by Multi-Ion-Beam Reactive Sputtering Technique," *Journal of Materials Research* **10**, 708-26 (1995).

22 Nye, J.F. *Physical Properties of Crystals*,(Clarendon, Oxford, 1957).

23 "Slide Motor," *product literature* (MCNC MEMS Technology Applications Center, http://mems.mcnc.org/figs/motor2.jpg.

24 Guckel, H. & MEMS, University of Wisconsin, "Micro Motor," (http://mems.engr.wisc.edu/image/motor/permalloy_motor.jpg, 1994).

25 Schulze, W.A. & Ogino, K. "Review of Literature on Aging of Dielectrics," *Ferroelectrics* **87**, 361-77 (1988).

26 Arlt, G. & Robels, U. "Aging and Fatigue in Bulk Ferroelectric Perovskite Ceramics," *Integrated Ferroelectrics* **3**, 343-49 (1993).

27 Wang, D., Fotinich, Y. & Carman, G.P. "Influence of Temperature on the Electromechanical and Fatigue Behavior of Piezoelectric Ceramics," *Journal of Applied Physics* **83**, 5342-50 (1998).

28 Ozgul, M.,"Electrochemical Phenomena in Piezoelectric Ceramics Leading to Polarization Fatigue," M. S. Thesis, *The Pennsylvania State University*, 1998.

29 Suo, Z. "Models for Breakdown-Resistance Dielectric and Ferroelectric Ceramics," *Journal of the Mechanical Physics of Solids* **41**, 1155-76 (1993).

30 Aburatani, H. & Uchino, K., "Destruction Mechanism and Destruction Detection Technique for Multilayer Ceramic Actuator," Proceedings of the Ninth IEEE International Symposium on Applications of Ferroelectrics 1995), 2, 750-2.

31 Hill, M., White, G.S., Hwang, C.-S. & Lloyd, I.K. "Cyclic Damage in Lead Zirconate Titanate," *Journal of the American Ceramic Society* **79**, 1915-20 (1996).

32 Cheon, C.-I., Kim, S.-J. & Kim, H.-G. "Electrically Induced Microcracking in Modified PZT Ceramics," *Ferroelectrics* **115**, 35-42 (1991).

33 Al-Shareef, H. & Dimos, D., "Accelerated Life-Time Testing and Resistance Degradation of Thin-Film Decoupling Capacitors," Proceedings of the Tenth IEEE International Symposium on Applications of Ferroelectrics (East Brunswick, NJ, 1996), 1, 421-5.

34 Munikoti, R. & Dhar, P. "Highly Accelerated Life Testing (HALT) for Multilayer Ceramic Capacitor Qualification," *IEEE Transactions on Components, Hybrids, and Manufacturing Technology* **11**, 342 - 45 (1988).

35 Rawal, B.S. & Chan, N.H., "Conduction and Failure Mechanisms in Barium Titanate Based Ceramics Under Highly Accelerated Conditions," *product literature* (AVX Corporation, Myrtle Beach, 1984).

36 Waser, R., Baiatu, T. & Hardtl, K.-H. "dc Electrical Degradation of Perovskite-Type Titanates: I. Ceramics," *Journal of the American Ceramic Society* **73**, 1645-53 (1990).

37 Waser, R., Baiatu, T. & Hardtl, K.H. "Degradation of Dielectric Ceramics," *Materials Science and Engineering* **A109**, 171-82 (1989).

38 Baiatu, T., Waser, R. & Hardtl, K.-H. "dc Electrical Degradation of Perovskite-Type Titanates: III. A Model of the Mechanism," *Journal of the American Ceramic Society* **73**, 1663-73 (1990).

39 Lee, J., Ramesh, R. & Keramidas, V.G. "Imprint and Oxygen Deficiency in $(Pb,La)(Zr,Ti)O_3$ Thin Film Capacitors with La-Sr-Co-O Electrodes," *Applied Physics Letters* **66**, 1337-39 (1995).

40 Pike, G.E., *et al.* "Voltage Offsets in $(Pb,La)(Zr,Ti)O_3$ Thin Films," *Applied Physics Letters* **66**, 484-86 (1995).

41 Budd, K.D., Dey, S.K. & Payne, D.A. "Sol-Gel Processing of $PbTiO_3$, $PbZrO_3$, PZT, and PLZT Thin Films," *British Ceramic Processing* **36**, 107-21 (1985).

42 Maria, J.-P.,"Epitaxial $Pb(Mg_{1/3}Nb_{2/3})O_3$-$PbTiO_3$ Thin Films," Ph. D. Thesis, *The Pennsylvania State University*, 1998.

43 Dimos, D., Warren, W.L., Sinclair, M.B., Tuttle, B.A. & Schwartz, R.W. "Photoinduced Hysteresis Changes and Optical Storage in $(Pb,La)(Zr, Ti)O_3$ Thin Films and Ceramics," *Journal of Applied Physics* **76**, 4305-15 (1994).

44 Warren, W.L., Dimos, D. & Waser, R. "Degradation Mechanisms in Ferroelectric and High Permittivity Perovskites," *MRS Bulletin* **July**, 40-5 (1996).

45 Warren, W.L., *et al.*, "Voltage Shifts and Defect Dipoles in Ferroelectric Capacitors," Materials Research Society Symposium: Ferroelectric Thin Films V (Boston, MA, 1996), 433, 257-66.

46 Warren, W.L., Dimos, D., Pike, G.E., Vanheusden, K. & Ramesh, R. "Alignment of Defect Dipoles in Polycrystalline Ferroelectrics," *Applied Physics Letters* **67**, 1689-91 (1995).

47 Kohli, M., Muralt, P. & Setter, N. "Removal of 90° Domain Pinning in (100) $Pb(Zr_{0.15}Ti_{0.85})O_3$ Thin Films by Pulsed Operation," *Applied Physics Letters* **72**, 3217-19 (1998).

48 Kholkin, A.L. & Setter, N. "Photoinduced Poling of Lead Titanate Zirconate Thin Films," *Applied Physics Letters* **71**, 2854-56 (1997).

49 Brody, P.S. & Crowne, F. "Mechanism for the High Voltage Photovoltaic Effect in Ceramic Ferroelectrics," *Journal of Electronic Materials* **4**, 955-71 (1975).

50 Lines, M.E. & Glass, A.M. "Principles and Applications of Ferroelectrics and Related Materials," in *The International Series of Monographs on Physics* (eds. Marshall, W. & Wilkinson, D.H.) 680 (Clarendon, Oxford, 1977).

51 Kurtz, S.K., Levinson, S. & Shi, D. "Infant Mortality, Freaks, and Wear-Out: Application of Modern Semiconductor Reliability Methods to Ceramic Multilayer Capacitors," *Journal of the American Ceramic Society* **72**, 2223-33 (1989).

52 Chan, N.H., Sharma, R.K. & Smyth, D.M. "Nonstoichiometry in Undoped $BaTiO_3$," *Journal of the American Ceramic Society* **64**, 556-62 (1981).

53 Gibbons, B.J.,"Real-Time Spectroscopic Ellipsometry and its Application to the Processing of $YBa_2Cu_3O_{7-\delta}$ Films by Molecular Beam Epitaxy," Ph. D. Thesis, *The Pennsylvania State University*, 1998.

54 Fowlkes, E.B. "Some Methods for Studying the Mixture of Two Normal (Lognormal) Distributions," *Journal of the American Statistical Association* **74**, 561-75 (1979).